

Master of Science Thesis in Electrical Engineering  
Department of Electrical Engineering, Linköping University, 2016

# Investigation of Control Approaches for a High Precision, Piezo-actuated Rotational Stage

**Niklas Ericson**



Master of Science Thesis in Electrical Engineering  
**Investigation of Control Approaches for a High Precision, Piezo-actuated  
Rotational Stage**  
Niklas Ericson  
LiTH-ISY-EX--16/4994--SE

Supervisor:   **Mark Butcher**  
                  CERN, Geneva, Switzerland  
**Pablo Serrano Galvez**  
                  CERN, Geneva, Switzerland  
**Måns Klingspor**  
                  ISY, Linköping University, Sweden

Examiner:     **Svante Gunnarsson**  
                  ISY, Linköping University, Sweden

*Division of Automatic Control  
Department of Electrical Engineering  
Linköping University  
SE-581 83 Linköping, Sweden*

Copyright © 2016 Niklas Ericson

## **Abstract**

The Equipment Controls and Electronics section (EN-STI-ECE) at CERN is developing a high precision piezo-actuated rotational stage for the UA9 crystal collimation project. This collaboration is investigating how tiny bent crystals can help to steer particle beams used in modern hadron colliders such as the Large Hadron Collider (LHC). Particles are deflected by following the crystal planar channels, "channeling" through the crystal. For high energy particles the angular acceptance for channeling is very low, demanding for a high angular precision mechanism, i.e. the rotational stage. Several control-related issues arising from the complexity and operational environment of the system make it difficult to design a controller that achieves the desired performance. This thesis investigates different control approaches that could be used to improve the tracking capability of the rotational stage. It shows that the IRC method could be used to efficiently control the rotational stage. Moreover it shows that a harmonic cancellation method could be used to increase the tracking accuracy by canceling known harmonic disturbances. The harmonic cancellation method (the RFDC) was implemented in this thesis and proposed as an add-on to the present control algorithm.



## Acknowledgments

First of all, I would like to thank CERN and the EN-STI-ECE section for giving me this opportunity. Especially my supervisors, Mark Butcher and Pablo Serrano Galvez, for interesting discussions and all the support that you have provided me with during my work with this thesis.

I would also like to thank my examiner Svante Gunnarsson and my supervisor Måns Klingspor at the Division of Automatic Control, Linköping University for your academic guidance and your flexibility in giving me support even though I have been located in Geneva.

Finally, I would like to express my gratitude to my friends and family and especially to my girlfriend Frida for your never ending support. Thank you all for encouraging me in my decision to move to Geneva. Without your love and support none of this would have been possible. Thank you.

*Geneva, August 2016  
Niklas Ericson*



---

# Contents

|   |           |
|---|-----------|
| <b>Notation</b>   | <b>ix</b> |
| <b>1 Introduction</b>   | <b>1</b>  |
| 1.1 Background . . . . .  | 1         |
| 1.2 Motivation . . . . .  | 2         |
| 1.3 Purpose and Goal . . . . .                                  | 2         |
| 1.4 Prospective Challenges . . . . .                            | 3         |
| 1.5 Related Work . . . . .                                      | 3         |
| 1.6 Method . . . . .  | 4         |
| 1.7 Limitations . . . . .                                       | 4         |
| 1.8 Outline . . . . .   | 5         |
| <b>2 System Overview</b>  | <b>7</b>  |
| 2.1 Crystal Collimators . . . . .                               | 7         |
| 2.2 Rotational Stage . . . . .                                  | 10        |
| 2.3 Piezoelectric Stack Actuators . . . . .                     | 11        |
| 2.3.1 Hysteresis Effect . . . . .                               | 11        |
| 2.3.2 Creep Effect . . . . .                                    | 11        |
| 2.4 Rotational Stage Modeling . . . . .                         | 12        |
| 2.4.1 Maxwell-slip Model . . . . .                              | 12        |
| 2.4.2 Linear System Identification . . . . .                    | 13        |
| 2.5 Present Control Approach . . . . .                          | 15        |
| <b>3 Theory</b>   | <b>17</b> |
| 3.1 Model Reference Adaptive Control . . . . .                  | 17        |
| 3.1.1 Perturbation Estimation . . . . .                         | 18        |
| 3.1.2 Adaptive Laws . . . . .                                   | 18        |
| 3.2 Integral Resonance Control . . . . .                        | 21        |
| 3.3 Harmonic Cancellation . . . . .                             | 23        |
| 3.3.1 Feedforward Disturbance Cancellation . . . . .            | 23        |
| 3.3.2 Cancellation with Internal Model Principle . . . . .      | 24        |
| 3.3.3 Repetitive Feedforward Disturbance Cancellation . . . . . | 25        |
| 3.3.4 Beat Effect . . . . .                                     | 28        |

|   |           |
|---|-----------|
| <b>4 Simulation Results</b>                                     | <b>29</b> |
| 4.1 Benchmarking Tests . . . . .                                | 29        |
| 4.2 Linear Dynamics Characterization . . . . .                  | 30        |
| 4.3 Model Reference Adaptive Control . . . . .                  | 32        |
| 4.4 Integral Resonance Control . . . . .                        | 39        |
| 4.5 Harmonic Cancellation . . . . .                             | 47        |
| 4.5.1 Feedforward Disturbance Cancellation . . . . .            | 47        |
| 4.5.2 Cancellation with Internal Model Principle . . . . .      | 52        |
| 4.5.3 Repetitive Feedforward Disturbance Cancellation . . . . . | 56        |
| 4.6 Comparison . . . . .  | 62        |
| <b>5 Experimental Results</b>                                   | <b>65</b> |
| 5.1 Setup . . . . .   | 65        |
| 5.1.1 Implementation . . . . .                                  | 65        |
| 5.2 Cancellation Verification . . . . .                         | 66        |
| 5.2.1 Single Disturbance . . . . .                              | 66        |
| 5.2.2 Multiple Disturbances . . . . .                           | 70        |
| 5.2.3 General Findings . . . . .                                | 72        |
| <b>6 Conclusion and Future Work</b>                             | <b>75</b> |
| 6.1 Conclusions . . . . .                                       | 75        |
| 6.1.1 Simulations . . . . .                                     | 75        |
| 6.1.2 Implementation . . . . .                                  | 77        |
| 6.2 Future Work . . . . .                                       | 78        |
| <b>A Simulation values</b>                                      | <b>81</b> |
| A.1 RFDC . . . . .  | 81        |
| A.2 Feedforward Disturbance Cancellation . . . . .              | 82        |
| <b>Bibliography</b>   | <b>83</b> |

---

# Notation

## ABBREVIATIONS

| Abbreviation | Meaning  |
|--------------|--|
| CERN         | European Council for Nuclear Research  |
| EN-STI-ECE   | Engineering Department - Source, Target and Interaction Group - Equipment and Controls Section |
| STM          | Scanning Tunneling Microscope  |
| AFM          | Atomic Force Microscope  |
| LHC          | Large Hadron Collider  |
| PEA          | Piezoelectric Actuator   |
| PID          | Proportional, Integral, Derivative (controller)  |
| DOF          | Degrees of Freedom   |
| PRBS         | Pseudo Random Binary Sequence  |
| TF           | Transfer Function  |
| QFT          | Quantitative Feedback Theorem  |
| FFT          | Fast Fourier Transform   |
| IRC          | Integral Resonance Control   |
| IMP          | Internal Model Principle   |
| RFDC         | Repetitive Feedforward Disturbance Cancellation  |
| MRAC         | Model Reference Adaptive Controller  |
| MRACPE       | Model Reference Adaptive Controller with Perturbation Estimation                               |
| FDC          | Feedforward Disturbance Cancellation   |
| GUI          | Graphical User Interface   |
| LVDT         | Linear Variable Differential Transformer   |
| PXI          | Peripheral component interconnect eXtensions for Instrumentation                               |



# 1

---

## Introduction

### 1.1 Background

High precision positioning systems are vital in for example scanning tunneling microscopes (STM), atomic force microscopes (AFM) and in semiconductor lithography. In AFM, for instance, high precision positioning is required to control the vertical position of the scanning probe to keep the force constant between the sample surface and the probe tip. A topographical image of the sample is obtained by raster-scanning the probe over the sample surface and plotting the vertical displacement against the probe's x-y position. A positioning system that keeps the force constant down to an atomic-scale resolution is thus inevitable in order to obtain a high resolution image without damaging the sample [6].

The piezoelectric effect is a phenomenon that arises in certain solid materials when an electric potential is generated in response to applied mechanical stress. The effect was first discovered by Jacques and Pierre Curie in 1880 when they found that applying pressure to a quartz crystal generates electrical potential. Today, it is commonly encountered in daily life and utilized in for example lighters, buzzers and loudspeakers. Smart materials such as the piezoelectric material are nowadays also used in precision actuators due to their ability to convert electrical energy into mechanical energy. Piezoelectric materials have been commercially available for almost 45 years and have become indispensable for the nanopositioning industry [7]. In cases where a relatively small displacement range is required (travel ranges up to 500  $\mu\text{m}$ ), a piezo electric device is the actuator of choice due to its fast response, high resolution and its ability to generate large mechanical forces for small amounts of power in compact designs [6].

The EN-STI-ECE section in the Engineering Department at CERN (European Organization for Nuclear Research) is developing a high precision positioning system for use in the UA9 crystal collimation study.

## 1.2 Motivation

Crystalline solids have the ability to constrain the directions that particles take as they pass through, commonly called the "channeling" property. The UA9 collaboration at CERN is investigating how tiny bent crystals can help to steer particle beams in modern hadron colliders such as the Large Hadron Collider (LHC) [22]. In high energy colliders particles tend to drift outwards creating a beam halo. These particles surrounding the beam might drift and cause damage to sensitive parts in the accelerator, such as the superconducting magnets which can suffer an abrupt loss in superconducting capability (quench) even from a small dose of deposited energy. To extract and absorb these halo particles, CERN uses a multi-stage collimation system, consisting of primary and secondary collimators connected in series. CERN's largest particle accelerator, the LHC operating at 7 TeV, has 108 collimators distributed along two beam pipes [18]. At the moment, these collimators use massive blocks of amorphous material to intercept with the beam and absorb halo particles. The UA9 experiment plans to develop a new collimator, utilizing the technique of a bent crystal and a single absorber which will, in theory, imply in a more efficient cleaning, a less complex system and a reduction of the machine impedance. These are all essential for reaching higher energy levels in a future particle accelerator.

## 1.3 Purpose and Goal

One major difficulty that arises with the use of bent crystals is that, the higher the energy of the particle, the lower the angular acceptance for channeling. Hence, a high precision rotational mechanism is required. For this purpose, the EN-STICE section is developing a rotational stage that will insert and rotate the crystal with a high angular accuracy. The purpose of this thesis is to identify possible control approaches that could be applicable to the rotational stage in order to achieve the desired performance. The stage is required to:

- have a total range of 20 mrad
- be able to track reference trajectories at ramp rates of 100  $\mu\text{rad/s}$
- reject external disturbances to maintain a maximum tracking error of  $\pm 1 \mu\text{rad}$  even when the linear axis is moving

## 1.4 Prospective Challenges

First of all, piezoelectric actuators show strong nonlinear properties such as hysteresis and creep (drift), which have to be compensated for [7]. Moreover, the mechanical flexural structure in the rotational stage in combination with the piezoelectric characteristics leads to a highly resonant structure, making it difficult to achieve the desired performance while operating the rotational stage within noisy environments with external disturbances such as ground vibrations. Furthermore, this rotational stage is attached to a linear stage which is composed of a lead-screw, a stepping motor and an axis. The linear movement adds additional perturbation to the rotational stage due to imperfections in the lead-screw and the detent torque and stepping nature of the motor [4]. Finally, the system changes drastically due to a number of factors such as linear position, linear speed and angular position in combination with a moving center of rotation. The linear dynamic modeling is thereby limited by all these factors requiring a controller that is robust to such variations.

## 1.5 Related Work

During the last couple of decades, a lot of research has been put into the area of nanopositioning and its applications. A well known application is the AFM discussed in [5, 6], where piezoelectric actuators are commonly used to position the scanning probe tip. The piezoelectric actuator is in many aspects the actuator of choice but its nonlinear characteristics make it hard to control. A lot of recently published reports discuss the control of piezoelectric actuator [14, 16] and also how to model and compensate for the nonlinear behavior [2, 3, 8, 17].

For the purpose of increasing tracking capability, disturbance rejection and model error robustness in the area of nanopositioning, a wide range of controllers have been reported with success. Many of these controllers either aim directly to suppress the nonlinear behavior [9, 20, 25] or to work in combination with a hysteresis cancellation method [15, 26].

For systems suffering from harmonic disturbances, control methodologies offering harmonic cancellation could be used to efficiently increase the overall tracking performance. Several methods exist where the harmonic cancellation is added either as a feedforward from the modeled disturbance [11, 24] or directly in the closed loop [27].

At CERN, a first approach has already been implemented to achieve the desired performance. The proposed controller, presented in [4] delivers reasonable performance but does not fulfill the requirements during movement. The authors proposes a PID controller in combination with a prefilter, and a hysteresis compensator. The controller has shown high disturbance rejection at the first resonance peak as well as good tracking performance.

## 1.6 Method

The plan of this thesis was to identify possible control approaches, benchmark them in simulations to confirm their applicability and implement the most promising one. The goal can thereby be summarized in the following two questions.

- What control approaches can be used to achieve the desired performance?
- Which one is the most promising approach with respect to simulated/benchmarked results and ease of implementation on the real device?

To provide answers to the above questions the following methodology has been used in this thesis.

- Literature study
- Further investigation of selected control approaches
- Benchmarking tests of selected control approaches in simulations
- Implementation of the most promising approach
- Proposal of controller

The literature study covered a large number of control approaches to give a good overview of advantages and disadvantages with available control methodologies. After the initial literature study, further investigation was conducted with the selected approaches. All selected approaches were benchmarked in simulations, carried out in Matlab and Simulink. Finally, with performance, stability and implementation considerations, one approach was selected and implemented in LabVIEW to operate on the real device. The final results were then used to verify the simulation performance and to give a final statement of the controller's applicability and effectiveness.

## 1.7 Limitations

This thesis has solely focused on control approaches and has thereby excluded all modeling of the system. Extensive modeling had already been carried out on the device, motivating the exclusion. Due to time limitations, only a few control approaches were selected for simulation and only one of them was implemented on the real device. For the same reason, all controller tuning were only carried out until a sufficient set of parameters was found i.e. a more optimal set of parameters could have existed at the time which would have implied in a even better controller performance.

All simulations will be performed on a linear system model, assuming perfect inverse hysteresis cancellation and a sufficient closed loop to compensate for the creep effect, motivated by the extensive hysteresis model. Furthermore, all controllers will be discretized with a 2 kHz sampling frequency for the sake of comparison, even though the number of operations might allow for a higher execution rate.

## 1.8 Outline

This thesis provides the reader with a detailed description of the system, related theory and simulation results of the selected control methodologies as well as implementation results from benchmarking tests with the selected harmonic cancellation approach. The overview presented in Chapter 2 provides a brief introduction to collimation and how collimators operate in the LHC and a more detailed description of the rotational stage including the nonlinear effects that origin from the piezoelectric material. Moreover, a description of the linear identification and the nonlinear compensation is presented in the same chapter as well as an explanation of the present control algorithm. In Chapter 3 the simulation results of each controller is presented individually, benchmarked only to the present system. This is followed by two comparison tables gathering comparable results from the different control methods, respectively. In Chapter 5 the experimental results from the implementation of the harmonic cancellation is presented and in Chapter 6 the work is concluded and final answers to the formulated questions are given.



# 2

---

## System Overview

This chapter provides the reader with a brief overview of the collimation system used in the LHC at CERN as well as a more detailed description of the rotational stage, which is the device in focus in this thesis. It also gives a short description of the piezoelectric actuator and its nonlinear effects. At the end of this chapter the present control approach is described in detail, including modeling of the rotational stage, system identification and controller structure.

### 2.1 Crystal Collimators

A collimator is a specially designed device, built to interfere with the beam and clean it from surrounding halo particles. To be able to meet the future demand of higher energy levels, a more efficient collimator is being developed at CERN. This new collimator, named goniometer, will utilize a crystalline solid to extract particles from the beam. A very simplified illustration of the crystal collimation principle is shown in Figure 2.1.

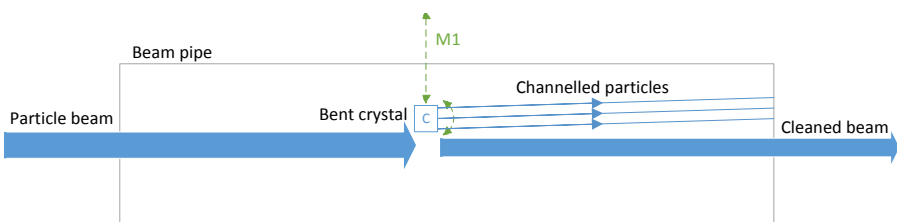


**Figure 2.1:** Illustration of the crystal collimation principle as seen from above (top view in Figure 2.3). The dashed lines represent the linear and rotational stage movement.

The block named "C" in Figure 2.1 represents the bent crystal which can be moved into the beam by the linear stage and rotated by the rotational stage which is attached to the linear axis. The crystal's linear and rotational movement are indicated in the figure as green dashed lines. During operation, physicists will drive the crystal close to the beam, enter it with an angle and rotate it slightly (in the range of 1 mrad) until the channeling effect is detected. Channeled particles (illustrated as arrowed lines in Figure 2.1) will then bend off from the beam core to be absorbed further down the beam pipe.

The goniometer unit consists of a T-shape structure containing two linear and one rotational stage, as partly illustrated in Figure 2.2.

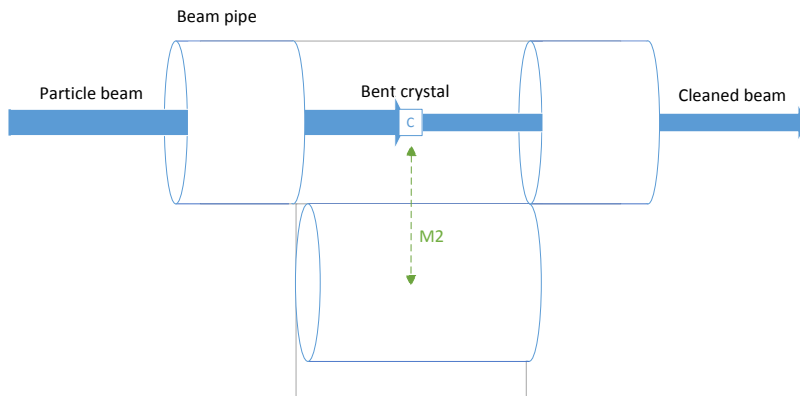


**Figure 2.2:** Illustration of the crystal collimation principle as seen from the side (side view in Figure 2.3). The green dashed line represents the movement of the beam pipe piece.

Each linear stage is driven by a stepping motor, labeled as  $M1$  in Figure 2.1 and  $M2$  in Figure 2.2, separately controlled in open-loop by an individual drive unit. The motor driving the vertical axis,  $M2$ , is used to move a piece of beam pipe inside the T-shape, giving access to the crystal to enter and to close it when the collimation system is out of operation. This movement is illustrated in Figure 2.2 with a green dashed line.

Figure 2.3 shows the new goniometer. In the top view the rotational and the linear horizontal stage is indicated with labels. In this figure, the rotational stage is in its outer position. During operation it will be moved forward by the linear axis into the beam pipe. Figure 2.4a shows the inside of the beam pipe during movement of the beam pipe piece, the same movement that Figure 2.2 is illustrating. In Figure 2.4b the crystal support has been injected into the beam pipe. Note that the crystal itself is in this picture replaced by a small circular mirror.

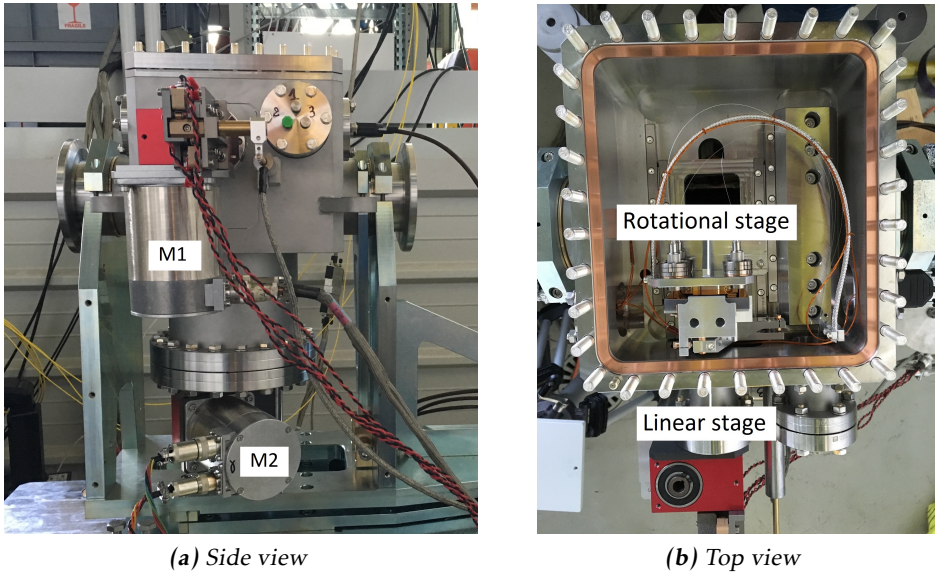


**Figure 2.3:** The new goniometer from the side (a) and the top (b).

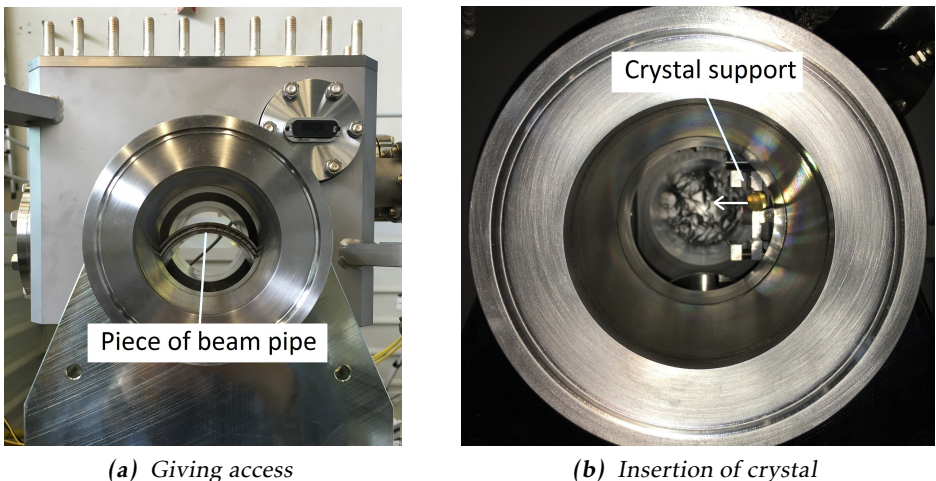


**Figure 2.4:** The new goniometer with the beam pipe piece half-way out (a) and the crystal inserted into the beam pipe (b).

## 2.2 Rotational Stage

The rotational stage as shown in Figure 2.5 is composed of a monolithic amplifying structure, a prestressed piezoelectric stack actuator and an interferometer measurement system. The flexure-hinge based structure, avoids sliding parts and thereby enhance precision by reducing the number of nonlinear effects (e.g. backlash and friction). A piezoelectric stack actuator is exploited to generate the rotational movement by interacting on a amplifying lever that applies the force on the rotational head a few millimeters from the center of rotation, marked as a white "X" in the picture. This amplifying structure gives the rotational stage a range of 20 mrad from a nominal linear range of 30  $\mu\text{m}$ . The PEA is prestressed in order to enhance the overall stiffness as well as keeping the stack in place. This combination leads to a clear resonant structure, due to the characteristics of the PEA and the flexure structure, demanding a properly designed controller.

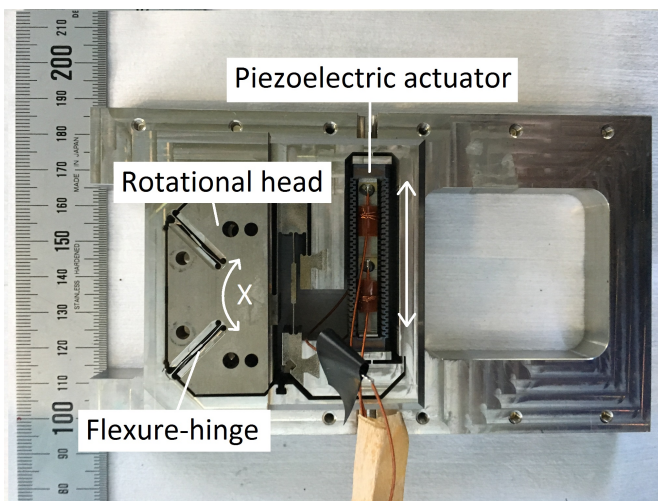


**Figure 2.5:** Piezo-actuated rotational stage used in the new goniometer.

For the measurement system, three interferometric heads are placed on top of the rotational stage as seen Figure 2.6, pointing towards a mirror that is attached to the crystal support and to the rotational head, perpendicular to the plane of rotation. The setup allows for measurements of both the yaw, depicted in Figure 2.5, and the roll angle (the coordinate system is defined with respect to the beam), but only the yaw angle is used in the feedback to the rotational stage control loop. Note that the crystal is mounted below the rotational head and that only the top of the crystal support is shown in the picture.

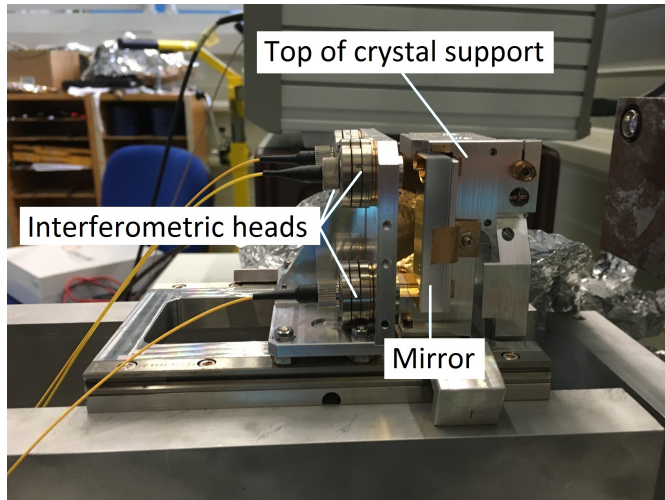


**Figure 2.6:** Rotational stage with the crystal support and the interferometric system mounted on top.

## 2.3 Piezoelectric Stack Actuators

The rotational stage uses a linear piezoelectric stack actuator to create the movement. It provides a displacement range from 0 to 30  $\mu\text{m}$ , corresponding to -20 and +150 V, respectively. The actuators are made of many thin, stacked electro-active ceramic disks, electrically connected in parallel. This construction allows for a high stiffness actuator that still can exhibit long displacement ranges [7].

### 2.3.1 Hysteresis Effect

The hysteresis effect is a nonlinear effect that is present during the operation of piezoelectric actuators. It occurs when the driving direction is reversed and originates from the polarization and the molecular effects in the piezo-ceramic. It depends on the amplitude of the applied voltage but also on the frequency of the input signal [19]. Figure 2.7a illustrates the hysteresis effect. One can see how the same voltage, e.g. 60 V, corresponds to an angular position of 5.2  $\mu\text{rad}$  in one direction and to 7.2  $\mu\text{rad}$  in the opposite direction.

### 2.3.2 Creep Effect

The creep effect is another nonlinear effect that is present during the operation of piezoelectric actuators. The effect is a slow elongation or contraction of the actuator displacement over time with a constant driving signal and is caused by thermal effects in the piezo-ceramics. Figure 2.7b illustrates the creep effect. One can see how the rotational stage slightly drifts off from the reference after the applied negative step, increasing the tracking error over time.

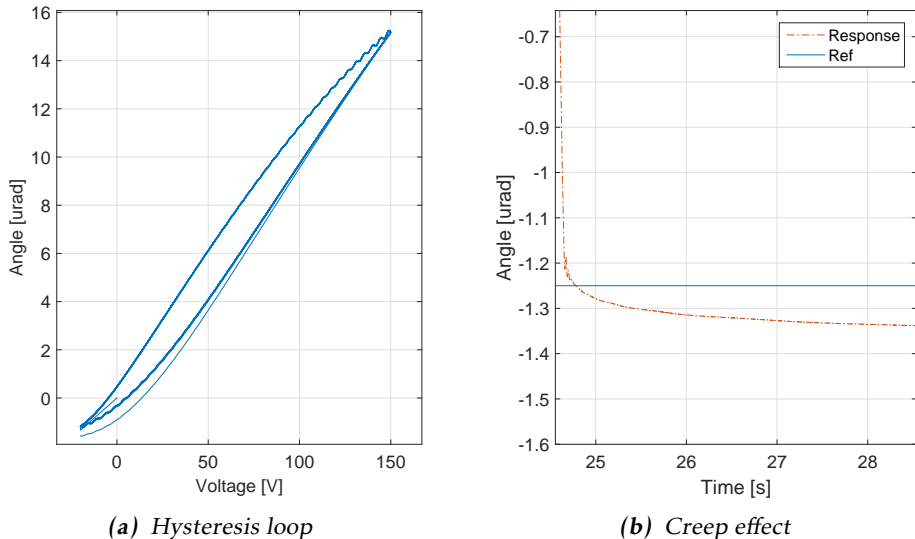


**Figure 2.7:** Illustration of the hysteresis effect (a) and creep effect (b). Note that the creep effect can last up to 10-15 minutes even if the plot only shows the development over 4 seconds.

The creep effect is in this project (and many others) efficiently suppressed by the feedback controller requiring no precise modeling and cancellation technique.

## 2.4 Rotational Stage Modeling

The piezo-actuated rotational stage is modeled by a Hammerstein structure, adopted by the authors in [4], allowing them in principal, to decouple the nonlinear hysteresis from the linear system dynamics. The employed Hammerstein structure is depicted in Figure 2.8 and consists of a *Static Hysteresis* (rate independent) model and a *Linear Dynamics* model. PEAs are known to show hysteretic behavior with a nonlocal memory (the current output does not only depend on the current input voltage but also on its history) as described in [3]. This behavior is modeled by a generalized Maxwell-slip compensation model, described in 2.4.1. The extracted linear dynamics is identified using the described procedure in 2.4.2.

### 2.4.1 Maxwell-slip Model

A generalized Maxwell-slip is used to model the hysteresis effect. It uses a parallel  $n^{th}$  order elasto-slide element system with a friction force acting on each

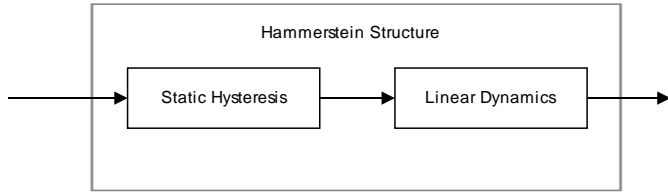


**Figure 2.8:** Block diagram of a Hammerstein structure, consisting of two blocks in series, modeling the static hysteresis and the linear dynamics, respectively.

element, to create a nonlinear model. An elasto-slide element consist of a massless spring connected in series with a massless block that is subject to Coulomb friction. The inverse hysteresis model is summarized in the following equations and described more thoroughly in [21],

$$F_i = \begin{cases} k_i(x - x_{bi}) & \text{if } k_i|x - x_{bi}| < f_i \\ f_i \operatorname{sgn}(\dot{x}) & \text{where } x = x_{bi} + \frac{f_i}{k_i} \operatorname{sgn}(\dot{x}) \\ & \text{else} \end{cases} \quad (2.1)$$

$$F = \sum_{i=1}^n F_i \quad (2.2)$$

where  $F_i$  is the output force,  $k_i$  the spring constant,  $f_i$  the break-away force and  $x_b$  is the block position where  $i = 1 \dots n$ . In terms of the rotational stage  $F_i$  represents the applied voltage,  $x$  the input (rotational) displacement,  $x_b$  angular position and  $k_i, f_i$  are unknown parameters. The model parameters have been estimated by fitting the model to the major hysteresis loop, obtained by acquiring data from the system with a 0.5 Hz input driving signal as described in [3, 4]. The identified set of parameters is presented in Table 2.1 where  $n = 10$ . The model fit of the hysteresis model, which uses the same set of parameters as the inverse hysteresis model, is shown in Figure 2.9.

## 2.4.2 Linear System Identification

The extracted linear dynamics have been identified as a 6<sup>th</sup> order transfer function using a PRBS as excitation signal, allowing for a valid extraction from the nonlinear dynamics. The system transfer function has been derived in discrete-time using the System Identification Toolbox in Matlab. A more detailed description of the procedure is available in [4]. The transfer function of the model (at 3.25 V), discretized with a sampling time of 0.5 ms, is presented in (2.3).

$$G(z) = \frac{21.05z^{-1} - 6.85z^{-2} + 8.52z^{-3} - 0.71z^{-4} + 9.30z^{-5}}{1344 - 2481z^{-1} + 1469z^{-2} + 21.64z^{-3} - 1767z^{-4} + 2084z^{-5} - 639.5z^{-6}} \quad (2.3)$$

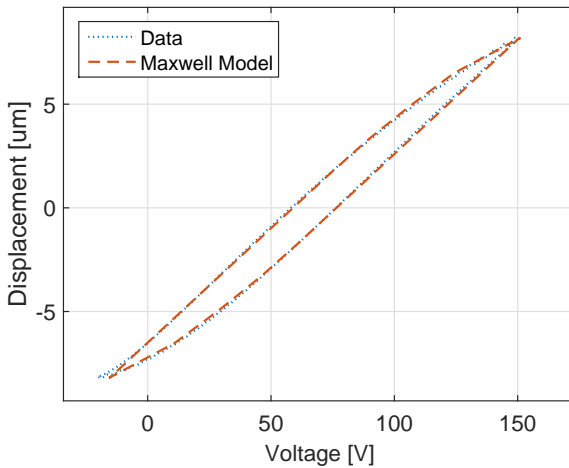


**Figure 2.9:** Model fit of the Maxwell slip model to the acquired hysteresis of the rotational stage.

| $i$ | $k_i$                 | $f_i$                 |
|-----|-----------------------|-----------------------|
| 1   | 4.53                  | 3.69                  |
| 2   | 0.90                  | 1.46                  |
| 3   | 1.01                  | 2.47                  |
| 4   | 0.36                  | 1.16                  |
| 5   | $1.49 \times 10^{-6}$ | $4.28 \times 10^{-6}$ |
| 6   | $2.89 \times 10^{-7}$ | $1.41 \times 10^{-6}$ |
| 7   | $1.59 \times 10^{-7}$ | $9.10 \times 10^{-7}$ |
| 8   | $1.39 \times 10^{-7}$ | $9.10 \times 10^{-7}$ |
| 9   | $2.28 \times 10^{-7}$ | $1.67 \times 10^{-6}$ |
| 10  | 4.58                  | 37.30                 |

**Table 2.1:** Identified parameters of the Maxwell slip model.

The transfer function uses five zeros and six poles to model two of the major resonances as seen in Figure 2.10, which shows a comparison between the model and the calculated Fast Fourier Transform (FFT) of the real system. The FFT was calculated by dividing the FFT of the output with the FFT of the input.

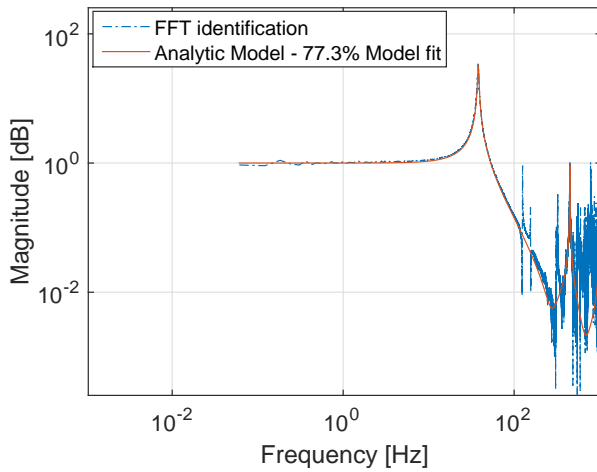


**Figure 2.10:** Model fit of the system model with 5 zeros and 6 poles shown in (2.3) to the FFT of the acquired data.

## 2.5 Present Control Approach

The original controller for the rotational stage is a 2-DOF structure (feedback and prefilter). A schematic overview of the control loop is depicted in Figure 2.11, consisting of a controller block C, a prefilter F, a disturbance d and the linearized rotational stage  $G = H^{-1}G_0$ , where  $G_0 = HG$  contains both the nonlinear and linear dynamics and  $H^{-1}$  is the hysteresis compensator.

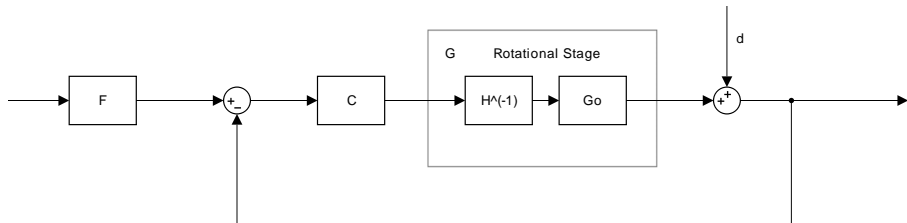


**Figure 2.11:** Block diagram of the present control loop, including controller, prefilter and hysteresis compensator.

The controller block (C) is a series combination of a PID controller, a notch filter and a lead filter, which stabilizes the system (PID), increases the phase margin (lead) and makes the system more robust to high frequency oscillations (notch). Since the open loop bandwidth is relatively low,  $f_b = 58$  Hz according to Figure 2.10, it was decided to exclude cancellation of the first resonance peak in order to maintain the bandwidth as high as possible and to have sufficient attenu-

ation of the first resonance peak [4]. Finally, to enhance the tracking performance, a prefilter ( $F$ ) was also added to the system. The PID controller, lead network, notch filter and prefilter are all presented below in (2.4).

$$F(z) = \frac{0.0029z - 0.0029}{z^3 - 2.91z^2 + 2.816z - 0.91} \quad (2.4a)$$

$$C_{PID}(z) = \frac{0.47z^2 - 0.94z + 0.47}{z^2 - 1.78z + 0.78} \quad (2.4b)$$

$$C_{lead}(z) = \frac{4.20z^2 - 7.72z + 3.55}{z^2 - 1.67z + 0.69} \quad (2.4c)$$

$$C_{notch}(z) = \frac{0.28z^4 - 0.62z^3 + 0.75z^2 - 0.59z + 0.26}{z^4 - 1.95z^3 + 1.39z^2 - 0.40z + 0.039} \quad (2.4d)$$

The effect of each filter can be seen in Figure 2.12a, where the open loop system is plotted with one filter added at a time. One can see that the high resonance peak is mitigated after the notch filter has been added, the lead filter rises the phase and that the PID controller provides good phase as well as good gain margin. Also the closed loop system is presented in Figure 2.12b, proving that the prefilter increases the closed loop bandwidth. The final closed loop bandwidth is 9.7 Hz.

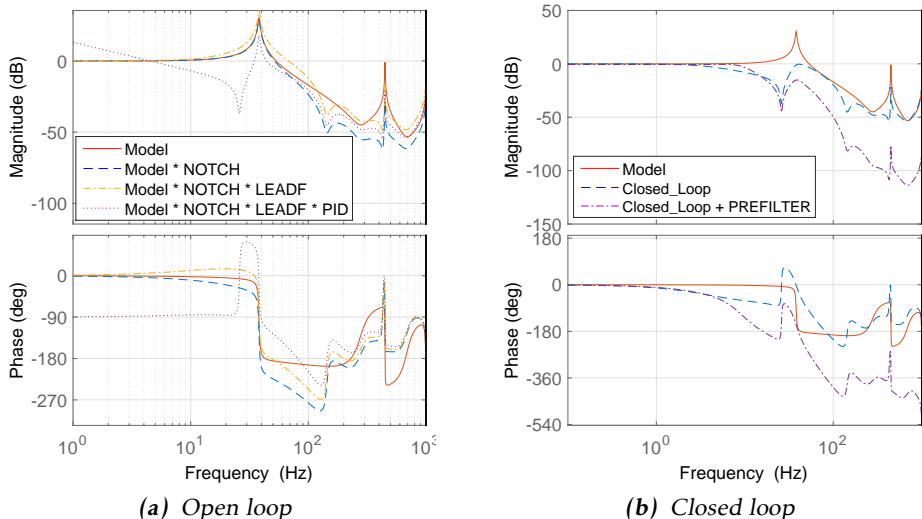


**Figure 2.12:** Illustration of controller effect. The effect of adding the different filters is shown in the open loop bode plot in (a) with the resulting closed loop system, with the open loop containing all filters, in (b).

# 3

---

## Theory

This chapter presents the motivation and the theory behind each of the control approaches investigated in this thesis. In the first two sections, an adaptive controller and an integral resonance controller is presented in detail. In the last and following section, harmonic cancellation is discussed, where three different approaches are described and motivated.

### 3.1 Model Reference Adaptive Control

An adaptive controller has the ability to adjust the system response by updating the parameters of a feedback controller in real time, resulting in a controller that is less sensitive to changes in the model and aging of the system. One approach is to use a reference model to create the desired system response which serves as a target for the adaptive laws. This approach is known as the Model Reference Adaptive Controller (MRAC). This model does not require any prior knowledge about the model uncertainties, implying a more straight-forward way to implement precision control to nanopositioning systems. Moreover, this scheme allows for the use of a lower order model (in relation to the system model) since the online parameter estimation can be used sufficiently with a lower order model. The MRAC scheme can be extended to include perturbation estimation (MRACPE), giving the controller the ability to compensate for various non-modeled effects, including both linear and nonlinear perturbations. Nonlinear effects such as the hysteresis are treated as lumped perturbations to the nominal system model and can be compensated for in the same manner as for linear disturbances, using the knowledge of the system and the previous measurement and output signal.

### 3.1.1 Perturbation Estimation

Using a second order model, the adaptive laws can be derived as follows. Consider the system model stated below.

$$\ddot{x}(t) + \alpha_1 \dot{x}(t) + \alpha_0 x(t) = \beta_0 u(t) + f(t) \quad (3.1)$$

where  $x(t)$  denotes the output angle at time  $t$ ,  $u(t)$  the input voltage at time  $t$  and  $\alpha_1, \alpha_0, \beta_0 \in \mathbb{R}$  are known system constants.  $f(t)$  is a function describing the unknown perturbations of the system, including the hysteresis and creep effect. The general equations for deriving the perturbation function are described more thoroughly in [9]. For a simple second order SISO-model the perturbation estimation becomes

$$\hat{f}(t) = \ddot{x}_{cal}(t) + \alpha_1 \dot{x}_{cal}(t) + \alpha_0 x(t) - \beta_0 u(t - T_s) \quad (3.2)$$

where  $x_{cal}^{(n)}$  denotes the calculated state of the  $n$ th order of time derivative,  $T_s$  is the sampling time interval and  $u(t - T_s)$  is the control input in the previous time step.  $u(t - T_s)$  is often approximated to  $u(t)$  in practice, which is a valid approximation if  $T_s$  is sufficiently small. Note that  $x(t)$  here is the sensor input, i.e. the measured yaw angle.

Each state is, for its computational efficiency, computed by a simple backward different equation depicted below.

$$x_{cal}^{(n)}(t) = \frac{x_{cal}^{(n-1)}(t) - x_{cal}^{(n-1)}(t - T_s)}{T_s} \quad (3.3)$$

### 3.1.2 Adaptive Laws

The objective of the adaptive laws is to calculate the control parameter so that they converge to ideal values resulting in a system response that matches the reference. The adaptive laws can be derived using Lyapunov theory which is outlined in this section. Consider the second order reference model below

$$\ddot{x}_m(t) + a_1 \dot{x}_m(t) + a_0 x_m(t) = b_0 u_d(t) \quad (3.4)$$

where  $x_m(t)$  denotes the output angle,  $u_d(t)$  the input voltage and  $a_0, a_1, b_0$  are known positive constants.

The tracking error is defined as below.

$$e(t) = x(t) - x_m(t) \quad (3.5)$$

Recalling (3.1), replacing  $f(t)$  with the estimation  $\hat{f}(t)$  and subtracting it from (3.4) gives the following expression where more details can be found in [19].

$$\ddot{e}(t) + a_1 \dot{e}(t) + a_0 e(t) = (a_1 - \alpha_1) \dot{x}(t) + (a_0 - \alpha_0) x(t) - b_0 u_d(t) - \beta_0 u(t) + \hat{f}(t) \quad (3.6)$$

Transforming it into state-space form

$$\dot{\mathbf{E}} = \mathbf{AE} + \beta_0 \mathbf{Bu} + \Delta \quad (3.7)$$

where

$$\mathbf{E} = \begin{bmatrix} e \\ \dot{e} \end{bmatrix}, \mathbf{A} = \begin{bmatrix} 0 & 1 \\ -a_0 & -a_1 \end{bmatrix}, \mathbf{B} = \begin{bmatrix} 0 \\ 1 \end{bmatrix}, \Delta = \begin{bmatrix} 0 \\ \delta \end{bmatrix} \quad (3.8)$$

with  $\delta = (a_1 - \alpha_1)\dot{x}(t) + (a_0 - \alpha_0)x(t) - b_0 u_d(t) + \hat{f}(t)$ .

If all eigenvalues of  $\mathbf{A}$  have negative real parts, then  $\mathbf{E}$  will tend to zero as  $t \rightarrow \infty$ , i.e. the system is asymptotically stable. Moreover, according to Lyapunov theory [13], for each positive-semidefinite matrix  $\mathbf{Q}$  there exists one positive-semidefinite matrix  $\mathbf{P}$  which solves (3.9).

$$\mathbf{A}^T \mathbf{P} + \mathbf{P} \mathbf{A} = -\mathbf{Q} \quad (3.9)$$

With the auxiliary item  $\hat{e} = \mathbf{E}^T \mathbf{PB}$ , the adaptive laws are given by

$$u = k_0 u_d + k_1 x + k_2 \dot{x} + k_3 \hat{f} \quad (3.10)$$

and the control law parameters are calculated as outlined below where  $\eta_i$  are tuning variables.

$$\dot{k}_0 = -\eta_0 \hat{e} u_d \quad (3.11)$$

$$\dot{k}_1 = -\eta_1 \hat{e} x \quad (3.12)$$

$$\dot{k}_2 = -\eta_2 \hat{e} \dot{x} \quad (3.13)$$

$$\dot{k}_3 = -\eta_3 \hat{e} \hat{f} \quad (3.14)$$

The proof can be found in [19]. Substituting  $\hat{f}$  in (3.2) with the one in (3.10) and rearranging the parameters result in the final MRACPE control law which is stated below.

$$u(t) = k_0 u_d(t) + (k_1 + k_3 \alpha_0)x(t) + (k_2 + k_3 \alpha_1)\dot{x}(t) + k_3 \ddot{x}(t) - k_3 \beta_0 u(t - T_s) \quad (3.15)$$

A block diagram of the final controller, with inspiration from Figure 9.1 in [19], is depicted in Figure 3.1. The adaptive controller consists of four blocks. One reference model that calculates the desired states  $\mathbf{x}_m = [\dot{x}_m, x_m]^T$  from the input signal according to (3.4), one adaptive mechanism that implements (3.11)-(3.14) and calculates  $\mathbf{k} = [k_1, k_2, k_3, k_4]^T$ , one state calculator that uses (3.3) to calculate  $\mathbf{x} = [\dot{x}, \dot{x}, x]^T$  and finally one controller block that uses (3.15) to calculate the control signal  $u$  that is sent to the rotational stage.

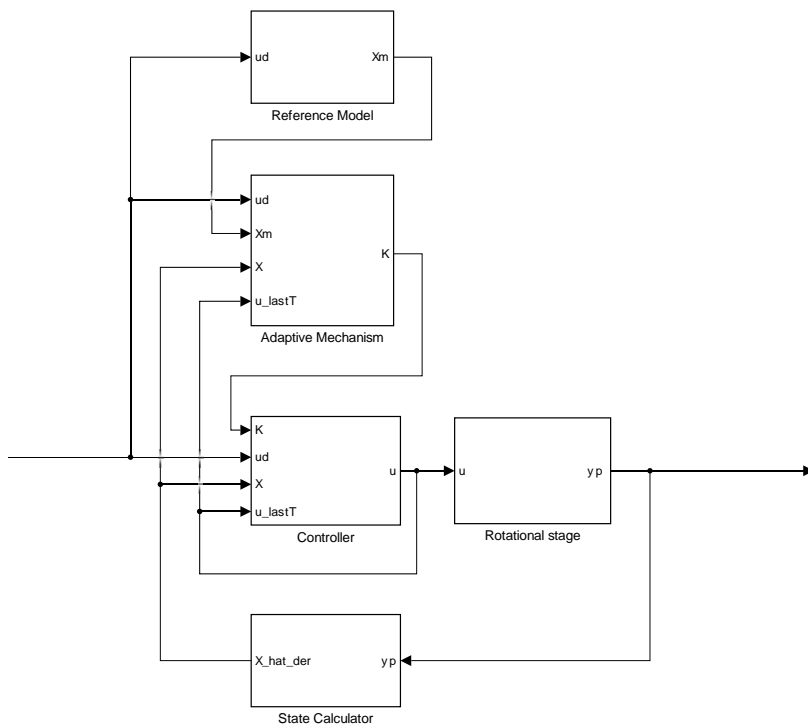


**Figure 3.1:** Block diagram of the adaptive controller

## 3.2 Integral Resonance Control

The integral resonance control (IRC) can be efficiently used to damp out the first resonant mode of the system, allowing for larger controller gains and a higher control bandwidth. The IRC block scheme is illustrated in Figure 3.2 and consists of a constant feed-through term  $D_f < 0$  and a negative integral controller  $C(s) = \frac{-k}{s}$  where  $k > 0$  for stability. The negative feedforward term will, if sufficiently large and negative, introduce a pair of complex zeros below the first resonance frequency and ensure zero-pole cancellation for higher resonance modes as shown in [1]. The addition of a negative feedforward will subtract, in the low frequency domain, a phase of  $-180^\circ$ . The phase margin can easily be increased by applying a simple negative integral controller to provide a  $90^\circ$  phase lead.

The negative gain  $D_f$  is straight-forward to manually select for introducing a complex pair of zeros below the first resonance. The integral gain  $k$  can be chosen by using the root locus technique and selecting a gain that maximizes damping.

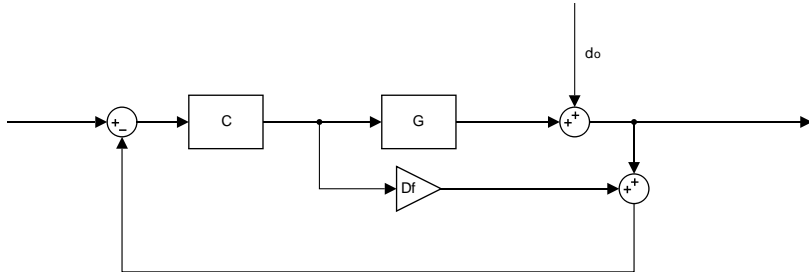


**Figure 3.2:** Block diagram of the IRC damping loop.

The IRC scheme in Figure 3.2 can be simplified, by combining  $C(s)$  and  $D_f$  in the same block, the resulting scheme is shown in the inner loop in Figure 3.3, where

$$C_2(s) = \left. \frac{C(s)}{1 + C(s)D_f} \right|_{C(s)=\frac{-k}{s}} = \frac{-k}{s - kD_f} \quad (3.16)$$

For tracking reference trajectories, the IRC can be enclosed in an outer loop, also seen in Figure 3.3, utilizing a second controller  $C_1(s)$  to compensate for disturbances and model errors [15]. The closed loop system ( $r$  to  $y$ ) and the sensitivity function ( $d_0$  to  $y$ ) for the IRC is written below.

$$G_c(s) = \frac{C_1(s)C_2(s)G(s)}{1 + C_2(s)G(s) + C_1(s)C_2(s)G(s)} \quad (3.17a)$$

$$S(s) = \frac{1}{1 + C_2(s)G(s) + C_1(s)C_2(s)G(s)} \quad (3.17b)$$

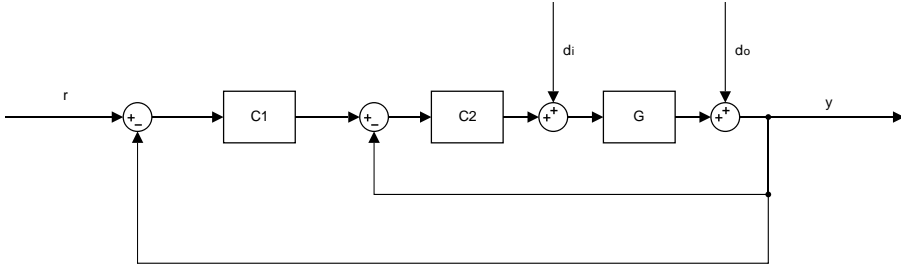


**Figure 3.3:** Block diagram of the tracking control system with IRC included.

Proof for the zero-pole entanglement and the insertion of the complex conjugate zeros can be found in [1], but note that the proof is only given for causal systems with a relative degree of two i.e two more poles than zeros.

To give the reader an intuitive explanation of the IRC and for a system with a relative degree of one, a brief example of a low order system is provided below. Let  $G$  be represented by a transfer function with a relative degree of one, with two poles and one zero as written below,

$$G(s) = \frac{s + \alpha_0}{s^2 + \beta_1 s + \beta_0} \quad (3.18)$$

where  $\alpha_i > 0$  and  $\beta_i > 0$ , i.e. a stable and minimum phase system. Using  $G_d(s) = G(s) + D_f$  (3.18) and rearranging the terms gives

$$\begin{aligned} G_d(s) &= \frac{s + \alpha_0}{s^2 + \beta_1 s + \beta_0} + D_f \\ &= \frac{D_f s^2 + (1 + D_f \beta_1)s + \alpha_0 + D_f \beta_0}{s^2 + \beta_1 s + \beta_0} \\ &= D_f \frac{s^2 + (\frac{1}{D_f} + \beta_1)s + \frac{\alpha_0}{D_f} + \beta_0}{s^2 + \beta_1 s + \beta_0} \end{aligned} \quad (3.19)$$

which illustrates that the number of introduced zeros is equal to the relative degree of the transfer function. Moreover, all zeros will have negative real part if the coefficients in  $s^2 + (\frac{1}{D_f} + \beta_1)s + (\frac{\alpha_0}{D_f} + \beta_0)$  are larger than zero i.e.  $\frac{1}{D_f} + \beta_1 > 0$  and  $\frac{\alpha_0}{D_f} + \beta_0 > 0$ . This can be simplified to the conditions given in (3.20).

$$\begin{cases} D_f < -\frac{1}{\beta_1} \\ D_f < -\frac{\alpha_0}{\beta_0} \end{cases} \quad (3.20)$$

## 3.3 Harmonic Cancellation

Cancellation of specific harmonics can be utilized to increase the regulation capability of a controller. A known or estimated disturbance can in many cases be efficiently eliminated by a number of methods [11, 12, 24]. Many of these approaches are based on the Internal Model Principle (IMP) meaning that the controller incorporates a known model of the disturbance within the control loop itself. However, including the disturbance model for effective cancellation in the feedback loop will deteriorate the sensitivity function. Although the sensitivity function is zero for selected frequencies, it is increased for other nearby frequencies, leading to severe damage in the total tracking accuracy. This phenomenon can be explained by Bode's integral constraints [13]. Hence, a feedforward approach is preferable to preserve the fine closed loop characteristics. For the sake of completeness, the IMP feedback approach is included in this chapter and evaluated in simulations to verify the expected results.

### 3.3.1 Feedforward Disturbance Cancellation

If a disturbance is measurable during operation, a feedforward of the disturbance model response can be used to eliminate the disturbance before it becomes present in the output signal [10]. A simple block diagram of the structure is shown in Figure 3.4, where  $G$ ,  $C$ ,  $P_d$  and  $K_f$  represent the system, the controller, the disturbance model and the feedforward block respectively.

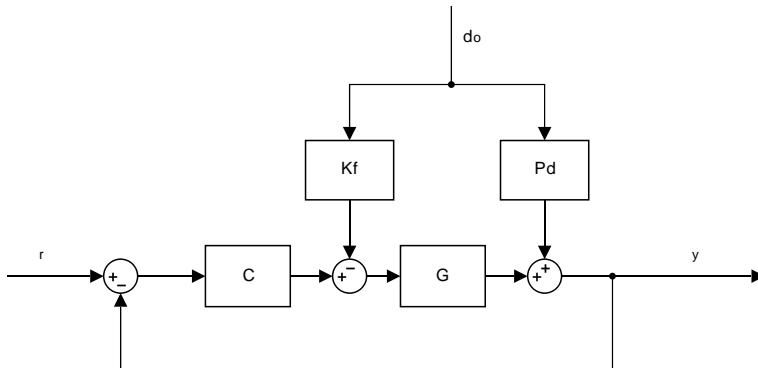


**Figure 3.4:** Block diagram of a control structure with feedforward from a known modeled disturbance.

The output is described by the following expression

$$Y(s) = \frac{C(s)G(s)}{1 + C(s)G(s)}R(s) + \frac{P_d(s) - K_f(s)G(s)}{1 + C(s)G(s)}D_0(s) \quad (3.21)$$

and hence an ideal choice of  $K_f(s)$  would be  $K_f(s) = P_d(s)/G(s)$  which would eliminate the disturbance completely. It is worth noting that the ideal  $K_f(s)$

might not be fully implementable (stable, proper and causal) and that the inverse of  $G(s)$  has to be approximated, leading to merely partial cancellation of the disturbance. This approximation can still be sufficient if the inverse is constructed in a way so that  $(P_d(s) - K_f(s)G(s))/(1 + C(s)G(s))$  becomes small for the frequencies where the disturbance has the most impact on the system.

### 3.3.2 Cancellation with Internal Model Principle

The IMP says that if a disturbance (entering the system on the output or input) can be described by a generating polynomial  $\Gamma(s)$  then a standard one DOF-controller  $C_t(s) = P(s)/(\Gamma(s)\bar{L}(s))$  can be used to asymptotically reject the effect of a modeled disturbance [27]. The generating polynomial  $\Gamma(s) = f(0, s)/D(s)$ , is derived by taking the Laplace transform of the differential equation describing the disturbance where  $f(0, s)$  arises from non-zero initial conditions. To show the principle of IMP parts of the evidence derived in [27] is presented here. Consider the system model  $G(s) = B(s)/A(s)$ . Using this system with the controller  $C_t(s)$  above in closed loop yields the sensitivity function in (3.22), which is the transfer function from output disturbance to output.

$$S(s) = \frac{A(s)\Gamma(s)\bar{L}(s)}{A(s)\Gamma(s)\bar{L}(s) + B(s)P(s)} \quad (3.22)$$

The system response to an output disturbance can then be derived as shown in (3.22).

$$Y(s) = S(s)D_o(s) = \frac{S(s)f(o, s)}{\Gamma(s)} = \frac{A(s)\bar{L}(s)}{A(s)\Gamma(s)\bar{L}(s) + B(s)P(s)}f(o, s) \quad (3.23)$$

The inverse Laplace transform  $y(t)$  converges to 0 if the controller has been tuned so that all roots to the characteristic polynomial  $A(s)\Gamma(s)\bar{L}(s) + B(s)P(s)$  have negative real parts. Hence, the disturbance is asymptotically rejected.

A basic block scheme is shown in Figure 3.5 where  $G(s)$  is the system,  $C(s) = P(s)/\bar{L}(s)$  the tunable controller,  $C_{imp}(s) = 1/\Gamma(s)$  is the compensator and  $d_o$  is the considered disturbance.

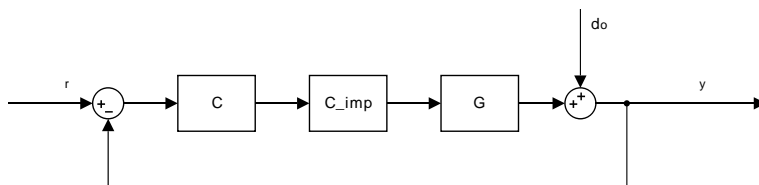


**Figure 3.5:** Block diagram of the IMP control structure.

### 3.3.3 Repetitive Feedforward Disturbance Cancellation

Repetitive control can be used to track and reject periodic disturbances with relatively long periods. For higher frequency modes, it fails to do so due to a number of reasons, but mostly for the inclusion of a low-pass filter, which is needed to maintain stability [11]. The conventional repetitive approach uses the IMP to include a discrete time disturbance model in the feedback controller. However, this approach will make the system more sensitive to other frequencies implying a reduction of the overall tracking capability. With respect to this drawback a novel control scheme with a feedforward switching mechanism and an observer was introduced by the authors in [12] for the purpose of head-tracking control in hard disk drives. This method is referred to as *Feedforward disturbance rejection with switching scheme* in the paper but will in this thesis simply be called RFDC (Repetitive Feedforward Disturbance Cancellation). A block diagram of the control scheme is presented in Figure 3.6, where  $G$  and  $C$  represent the system and the feedback controller as before. The output disturbance and the observed and replicated compensation signal are denoted  $d_o$  and  $d_i$ , respectively.

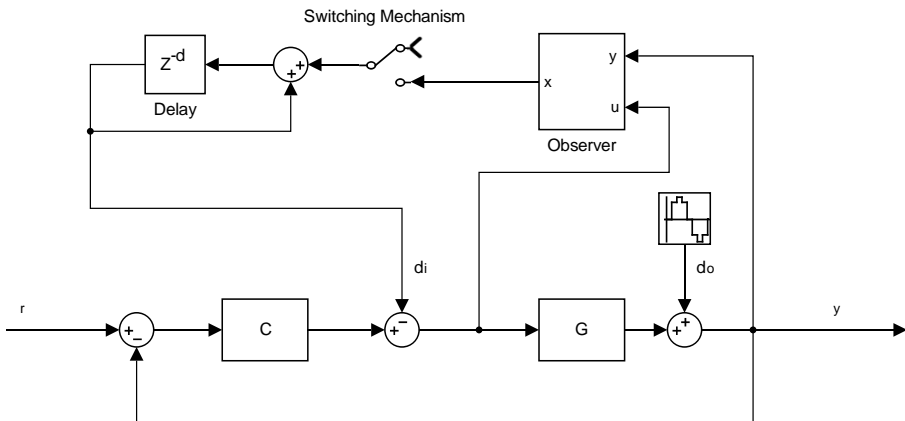


**Figure 3.6:** Block diagram of a feedforward switching mechanism including an observer and a feedback controller.

This method uses an observer to estimate the states of the disturbance. When the states have converged the switch is turned on for one period  $T_d$  of the disturbance. This period is then replicated and used to subtract the disturbance from the input signal as illustrated in the block diagram. The delay constant  $d$  and the switching on and off time have to be set in advance, hence  $T_d$  must be known. Note that if the disturbance frequency is not a multiple of the sampling frequency  $T_s$  then extra care has to be taken when setting the delay and switching times. Multiple periods should preferably be used to get a full number of oscillations within the switching timespan that is switched with a period of  $T_s$ .

The continuous time system in [12] is defined with  $d_o$  added on the input.

External disturbances are better modeled as disturbances added to the system output and therefore this approach has changed the position of  $d_o$ . However, the observer should still be modeling  $d_o$  as if it would be added to the input (see (3.24a)) to maintain cancellation of the harmonics at the input of the system. This assumes that  $G$  is linear and that the disturbance is sufficiently described by a sinusoidal, since a sinusoidal passing through a linear system only changes in phase and magnitude.

Using a continuous time state space representation, the system and the disturbance can be described as follows

$$\dot{\mathbf{x}}(t) = \mathbf{A}_c \mathbf{x}(t) + \mathbf{B}_c(u(t) + d_o(t)) \quad (3.24a)$$

$$y(t) = \mathbf{C}_c \mathbf{x}(t) \quad (3.24b)$$

and the disturbance as

$$\dot{\mathbf{x}}_d(t) = \mathbf{A}_d \mathbf{x}_d(t) \quad (3.25a)$$

$$d_o(t) = \mathbf{C}_d \mathbf{x}_d(t) \quad (3.25b)$$

where  $\mathbf{x}$  and  $\mathbf{x}_d$  are the system and disturbance state vectors and  $\mathbf{A}_c$ ,  $\mathbf{B}_c$ ,  $\mathbf{A}_d$ ,  $\mathbf{C}_c$  and  $\mathbf{C}_d$  are known system and disturbance matrices. The one-sided Laplace transform of  $\frac{1}{w} \sin(wt)$  is  $1/(s^2 + w^2)$ , which yields the state space equations in (3.26) with zero input.

$$\mathbf{A}_d = \begin{bmatrix} 0 & 1 \\ -w^2 & 0 \end{bmatrix} \quad \mathbf{C}_d = \begin{bmatrix} 1 & 0 \end{bmatrix} \quad (3.26)$$

The discrete time state space representation is obtained by using (3.27) from [10]

$$\mathbf{A}_z = e^{\mathbf{A}T_s} \quad \mathbf{B}_z = \int_0^{T_s} e^{\mathbf{A}T_s} \mathbf{B} dt \quad \mathbf{C}_z = \mathbf{C} \quad (3.27)$$

yielding the equations in (3.28)

$$\mathbf{x}_{zs}[n+1] = \mathbf{A}_{zs} \mathbf{x}_{zs}[n] + \mathbf{B}_{zs}(u_z[n] + d_{zo}[n]) \quad (3.28a)$$

$$y_{zs}[n] = \mathbf{C}_{zs} \mathbf{x}_{zs}[n] \quad (3.28b)$$

$$\mathbf{x}_{zd}[n+1] = \mathbf{A}_{zd} \mathbf{x}_{zd}[n] \quad (3.28c)$$

$$d_{zo}[n] = \mathbf{C}_{zd} \mathbf{x}_{zd}[n] \quad (3.28d)$$

where the disturbance and input are assumed to be piecewise constant during each sampling period  $T_s$ .

The disturbance is estimated by an observer which is given as

$$\hat{x}[n+1] = \mathbf{A}\hat{x}[n] + \mathbf{B}u[n] + \mathbf{K}(\mathbf{y}[n] - \mathbf{C}\hat{x}[n]) \quad (3.29)$$

where  $\mathbf{A}$ ,  $\mathbf{B}$  and  $\mathbf{C}$  are the augmented system matrices and  $\mathbf{K}$  is the observer gain.

$$\mathbf{A} = \begin{bmatrix} \mathbf{A}_{zs} & \mathbf{C}_{zd}\mathbf{B}_{zs} \\ \mathbf{0} & \mathbf{A}_{zd} \end{bmatrix} \quad \mathbf{B} = \begin{bmatrix} \mathbf{B}_{zs} \\ \mathbf{0} \end{bmatrix} \quad \mathbf{C} = \begin{bmatrix} \mathbf{C}_{zs} & \mathbf{0} \end{bmatrix} \quad (3.30)$$

The observer gain should be tuned (placing the eigenvalues of  $\mathbf{A} - \mathbf{KC}$ ) with respect to the trade-off between the convergence rate in the state reconstruction and the sensitivity to measurement noise. An optimal choice of  $\mathbf{K}$  can be calculated by the Kalman filter if the noise intensities are known. By deriving the closed loop system, it is shown in [12] that the disturbance rejection will be achieved at every sampling point in steady state.

The method can be extended to estimate and reject  $n$  harmonics by extending  $\mathbf{A}_d$  as shown in (3.31), adding  $n$  delay loops for each estimated disturbance and by summing all replicated disturbances i.e.  $d_i = \sum_{k=1}^n d_k$ .

$$\mathbf{A}_{de} = \text{diag} \left( \begin{bmatrix} \mathbf{A}_{d1} & \mathbf{A}_{d2} & \dots & \mathbf{A}_{dn} \end{bmatrix} \right) \quad \mathbf{C}_{de} = \begin{bmatrix} \mathbf{C}_{d1} & \mathbf{C}_{d2} & \dots & \mathbf{C}_{dn} \end{bmatrix} \quad (3.31)$$

To reduce the amount of non-modeled disturbances entering the disturbance estimation, the authors in [12] suggest a bandpass filter to be added after the replication. This could be any type of bandpass filter but it needs to have zero-phase for the selected frequencies, making the range of applicable filters much more narrow. One example of bandpass filter, with zero phase for the selected frequency  $\omega$  is

$$BP = k \frac{s^2 + 2\xi_a \omega s + \omega^2}{s^2 + 2\xi_b \omega s + \omega^2} \quad (3.32)$$

which has to be discretized before implementation.

### 3.3.4 Beat Effect

When cancelling one harmonic with another, one might encounter an oscillating effect in the performance known as the "beat effect". A beat is an interference pattern that occurs due to constructive and destructive interference between two signals that propagate with slightly different frequencies. The summation of the two signals forms an envelope, oscillating with a frequency of half the difference between the two frequencies [23]. Assume two signals with amplitude one and frequencies  $f_1$  and  $f_2$  i.e.  $y_1 = \cos(2\pi f_1 t)$  and  $y_2 = \cos(2\pi f_2 t)$ . Adding these signals and using trigonometric identities yields

$$y_1 + y_2 = 2\cos\left(2\pi \frac{f_1 + f_2}{2} t\right)\cos\left(2\pi \frac{f_1 - f_2}{2} t\right) \quad (3.33)$$

where the last cosine describes the envelope which oscillates with the frequency  $f_{beat}$  shown below.

$$f_{beat} = \frac{f_1 - f_2}{2} \quad (3.34)$$

# 4

---

## Simulation Results

This section describes the simulation results considering performance, robustness and stability with respect to the different control approaches. All approaches will first be benchmarked with the present control approach and presented individually in the following subsections. Comparison tables outlining the performance and the robustness of each controller will be presented in the end of this chapter.

### 4.1 Benchmarking Tests

For the comparison with the present control approach, all evaluated controllers were discretized with a sampling frequency of 2kHz. The normalized system in (2.3) was used to model the rotational stage linear dynamics. The nonlinear dynamics, creep and hysteresis, were neglected in the simulations, assuming perfect inverse hysteresis cancellation and a sufficient closed loop to compensate for the creep effect. All simulations were performed in Matlab and Simulink. The MRACPE and the IRC have been evaluated with respect to robustness to model errors, disturbance rejection, closed loop bandwidth and response to step and periodical input, all listed below.

- **Step and periodical tracking** - A step and a periodical input is applied to the input to benchmark the tracking capability of the controller.
- **Disturbance rejection** - Impulses are added to the input and output signal of the system to benchmark how sensitive the system is to system disturbances.
- **Robustness to model errors** - The robustness to model errors is characterized by changing the plant model but keeping the model in the controller constant.

The IMP, the FDC and the RFDC have been evaluated with respect to cancellation effectiveness and robustness to model errors, as listed below.

- **Cancellation performance** - Sinusoidal signals or acquired noise from the laboratory is added as disturbance to test the cancellation performance.
- **Robustness to model errors** - The robustness to model errors is characterized by changing the plant model of the system but keeping the model in the controller constant.

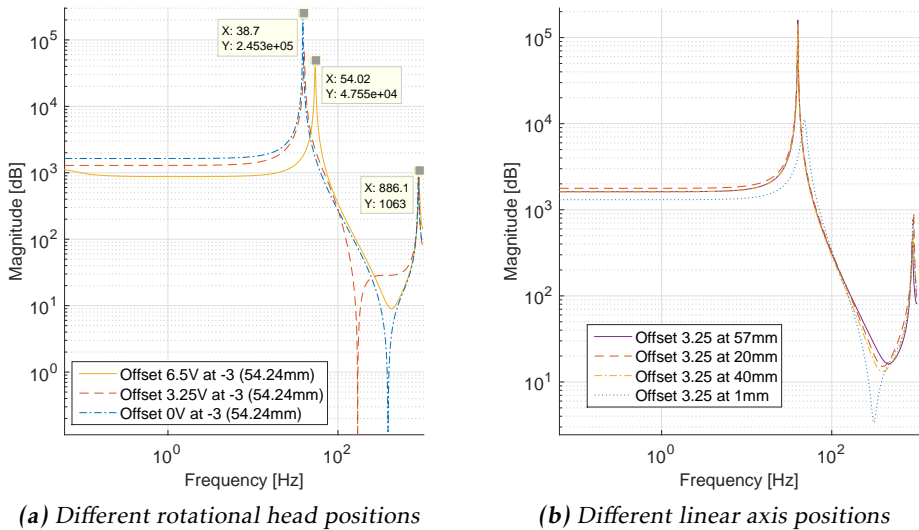
The prospective challenges, described in 1.4 shall be kept in mind while reading the results. Since the required ramp rates are relatively low, the disturbance rejection and the robustness to model errors are more of interest when evaluating each method.

## 4.2 Linear Dynamics Characterization

The linear dynamics of the rotational stage change due to a number of physical properties of the system, such as the current yaw-position, the linear axis position and speed and if the system is in contact with the end-switches. This phenomenon were characterized in a number of tests on a similar rotational stage as the one used for the simulations in this thesis. Figure 4.1a shows a comparison of the identified model when the linear axis is in its inner position and the rotational head has rotated -10 mrad (0 V), 0 mrad (3.25 V) and 10 mrad (6.5 V). It shows that the system changes its first resonance peak as much as 15.3 Hz.

Figure 4.1b shows a comparison of the identified model when the rotational head is in 0 mrad (3.25 V) and the linear axis position is in 1, 20, 40 and 57 mm. The identified system are almost the same for the first 3 positions, but it changes drastically when the linear axis is 1 mm from the switches i.e. in 57 mm.

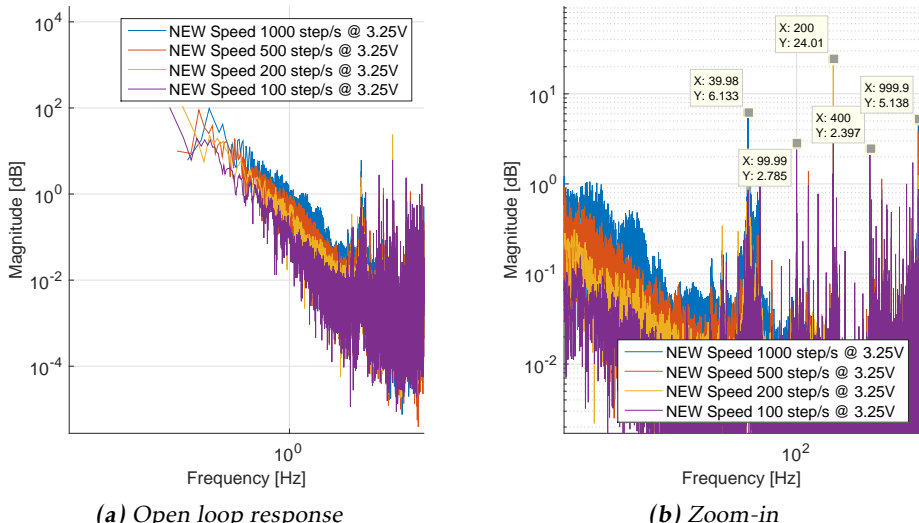
Since the rotational stage controller needs to maintain the required tracking error even when the linear axis is moving, the disturbance during linear movement must be considered. Figure 4.2 shows the open loop response when the linear axis is moving. This figure shows how the operating speed of the stepping motor influences the spectrum of the angle with its different harmonics.



(a) Different rotational head positions

(b) Different linear axis positions

**Figure 4.1:** Identified models with different rotational positions (linear axis in 54.24 mm) is shown in (a) and with different linear axis positions (rotational position corresponding to 3.25 V) is shown in (b).



(a) Open loop response

(b) Zoom-in

**Figure 4.2:** FFT of the yaw angle in open loop with the rotational head in 0 mrad (3.25 V). The whole spectrum is shown in (a) while a zoom-in is shown in (b). One can see how the induced harmonics are multiples of the stepping speeds.

## 4.3 Model Reference Adaptive Control

Even though a high order model of the rotational stage exists as presented in (2.3), a second order model approximating the higher order system was used in the adaptive control laws to keep the computational burden low. The discretized reference model can be seen in (4.1) and all parameters and tuning variables are summarized in Table 4.1. The controller was tuned to be robust to input disturbances and model changes. The set of parameter presented in Table 4.1 is not an optimal set but a decent set of parameters that maintains stability for step sizes below 20 mrad.

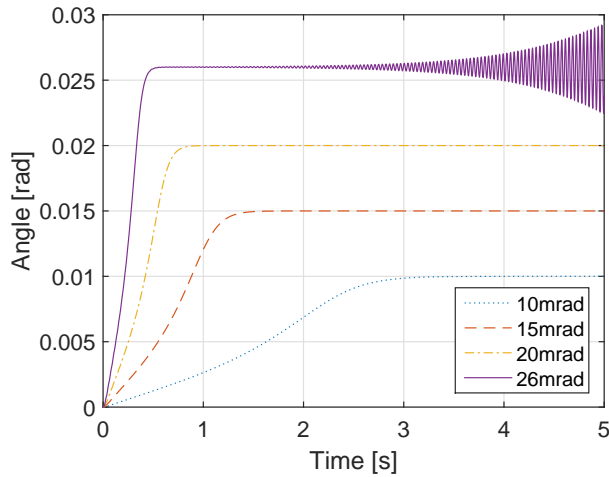
$$G_m(z) = \frac{7.9z + 6.7}{1313z^2 - 2095z + 796.4} \quad (4.1)$$

| Parameter  | Value                                      |
|------------|--|
| $T_s$      | $5 \times 10^{-4}$                         |
| $\alpha_0$ | $5.7 \times 10^4$                          |
| $\alpha_1$ | 7.2  |
| $\beta_0$  | $7.5 \times 10^7$                          |
| $a_0$      | $5.7 \times 10^4$                          |
| $a_1$      | $1 \times 10^3$                            |
| $b_0$      | $7.5 \times 10^7$                          |
| $\eta_0$   | $3 \times 10^{-2}$                         |
| $\eta_1$   | $1 \times 10^{-1}$                         |
| $\eta_2$   | $1 \times 10^{-10}$                        |
| $\eta_3$   | $1 \times 10^{-17}$                        |
| $\epsilon$ | $1 \times 10^{-8}$                         |
| $Q$        | $diag(1 \times 10^{10}, 1 \times 10^{-3})$ |

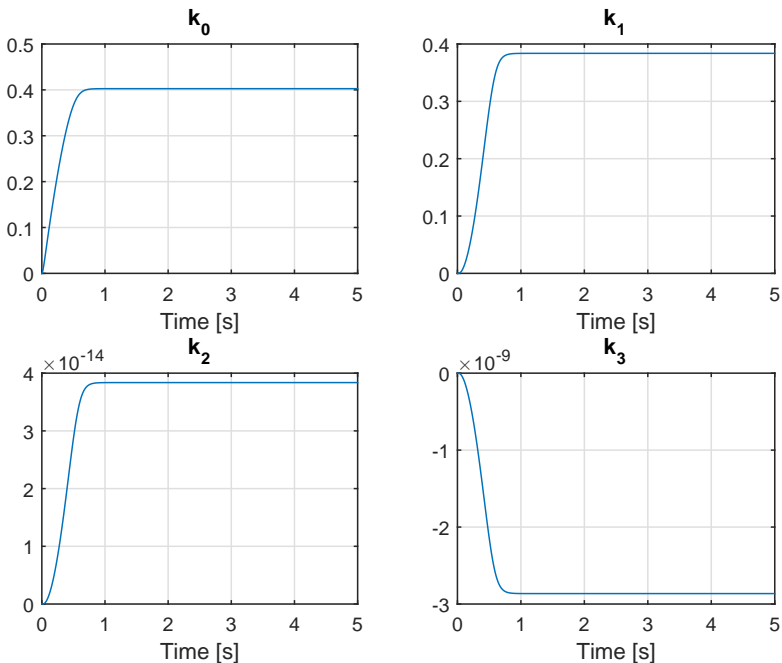
**Table 4.1:** Parameters of the system model and the tuned adaptive controller.

Figure 4.3 shows the step response to different step sizes. Here it is clear that the system becomes unstable if the step size  $\geq 26$  mrad. Note that all tests were produced with initial values  $k_i = 0$ .

The adaptation process of the control parameters  $k_i$ , for a step response resulting from a 20 mrad step, can be seen in Figure 4.4. All of the coefficients have converged within 1 s.



**Figure 4.3:** Step responses to step sizes of 10, 15, 20 and 26 mrad. The largest step illustrates a nonlinear phenomenon i.e. the controller stability depends on the step size.



**Figure 4.4:** Adaptation process of control parameters  $k_i$  with a 20 mrad step.

To illustrate the adaptation process better, a periodic response is depicted in Figure 4.5 which shows that after the adaptation process is finished the controller performs better for the second and third period. One can see that the adaptation process is slower for the periodic response corresponding to a lower step. Hence, the lower the step, the longer the adaptation time. The present controller tracks the periodic input well independently of the step size.

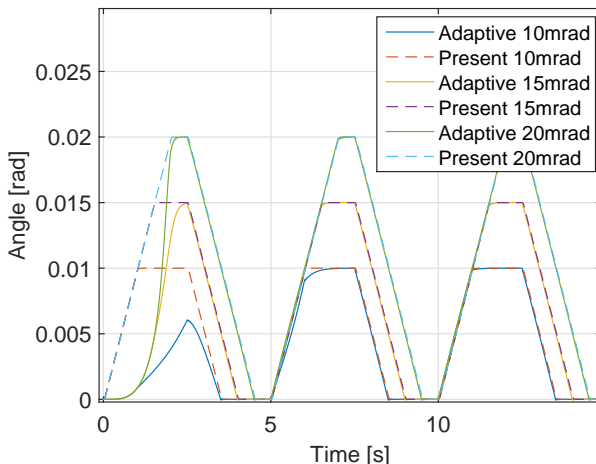


**Figure 4.5:** Periodical input response of the adaptive and the present controller with amplitudes of 10, 15, 20 mrad.

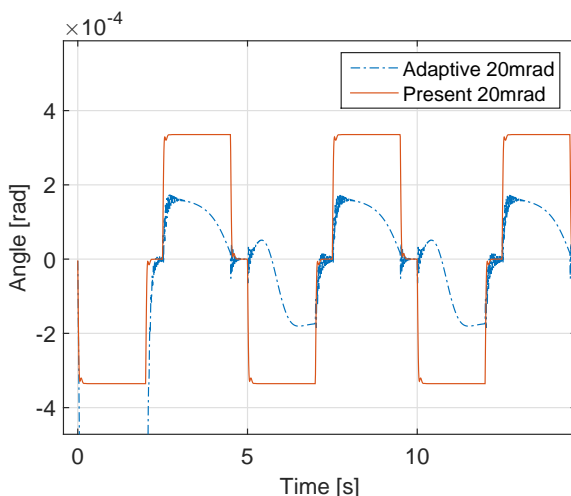
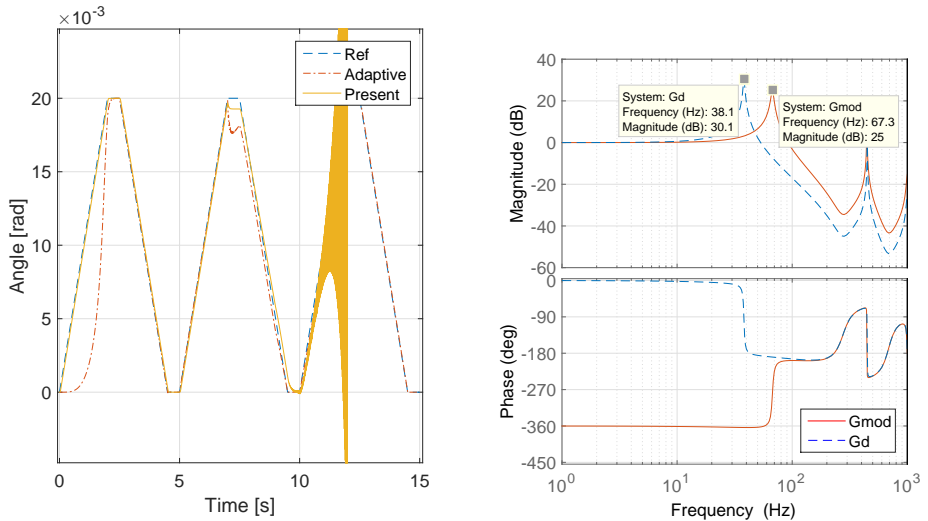


**Figure 4.6:** Tracking error (difference between the reference and output signal) of the periodical input response with an amplitude of 20 mrad.

The tracking error corresponding to the *Adaptive 20mrad* and *Present 20mrad* in Figure 4.5 can be seen in Figure 4.6. The adaptive controller performs better than the present controller after the adaptation process has finished.

A periodic response with model parameter drift is presented in Figure 4.7. It shows how the adaptive controller manages to adapt to changes in the plant, while the present controller fails to do so, resulting in an unstable system. The change of the model was performed over 2 seconds, resulting in a movement of the first resonance peak, from 38 Hz to 66 Hz in frequency and from 30.1 dB to 23.5 dB in magnitude.

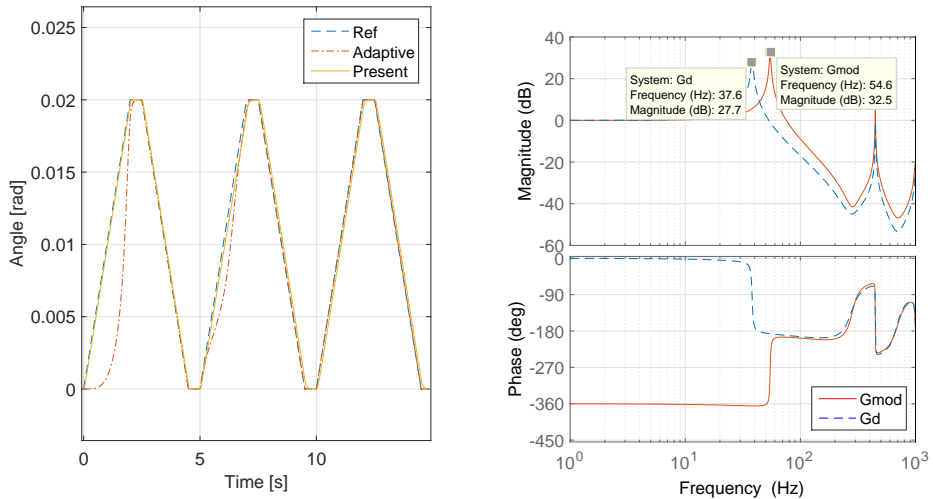


(a) Periodic response with model parameter drift.

(b) Original model ( $G_d$ ) and the resulting model after drift ( $G_{mod}$ ).

**Figure 4.7:** Periodical input response with induced model errors for the adaptive and the present controller. The model error is increased linearly from  $t = 7$  s to  $t = 9$  s. The resulting responses are shown in (a) with the induced model change in (b).

In the case in Figure 4.8 the resonance peak is only moved by 17 Hz and the present controller is sufficient to suppresses the disturbance. It even does it more efficiently than the adaptive controller. Even though the adaptive controller is slower than the present controller it still achieves a smaller tracking error after the adaption process is over, see Figure 4.9. Note that the change in the model is equivalent to the change between 0V and 6.5V presented in Figure 4.1a.



(a) Periodic response with model parameter drift.

(b) Original model ( $G$ ) and the resulting model after drift ( $G_{mod}$ ).

**Figure 4.8:** Periodical input response with induced model errors for the adaptive and the present controller. The model error is increased linearly from  $t = 5$  s to  $t = 7$  s. The resulting responses are shown in (a) with the model change in (b).

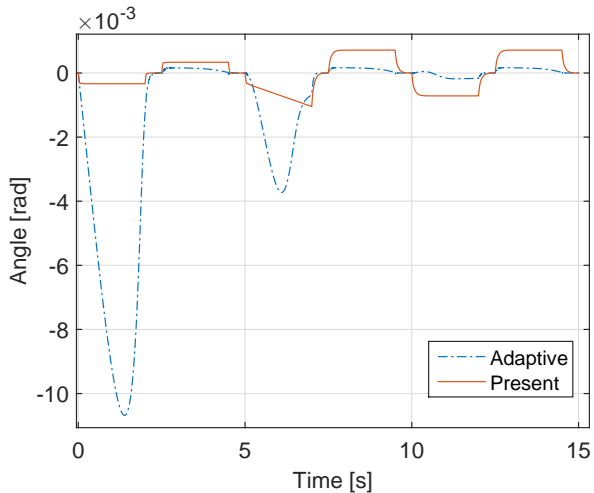


**Figure 4.9:** Tracking error of the periodic response with model errors increased linearly from  $t = 5$  s to  $t = 7$  s shown in Figure 4.8.

Figure 4.10 and 4.11 show the disturbance rejection capability to a disturbance applied on the input and output of the system. In Figure 4.10 a small impulse was added to the input. The adaptive controller performed worse than the present controller, attenuating the highest peak of the impulse by 62% less than the present. The settling time was also approximately 3 times longer for the adaptive controller. In Figure 4.11 the impulse was instead added to the output of the system. Even in this case the present controller was superior, attenuating the highest peak of the impulse by 43% more than the adaptive controller.

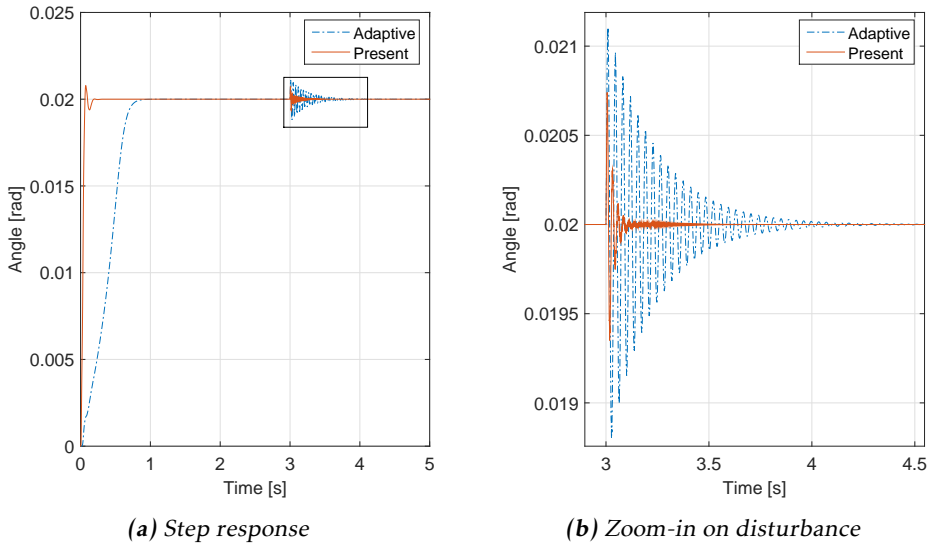
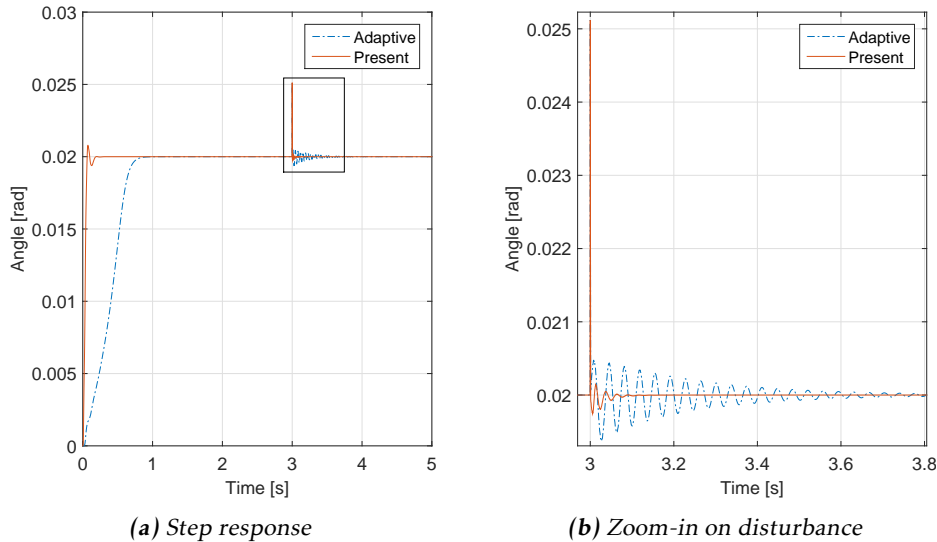


**Figure 4.10:** Step response with a disturbance impulse (amplitude of 5.1 mV) added to the input of the system at  $t = 3$  s. The whole step response is shown in (a) with a zoom-in on the disturbance in (b).



(a) Step response

(b) Zoom-in on disturbance

**Figure 4.11:** Step response with a disturbance impulse (amplitude of 5.1 mrad) added to the output of the system at  $t = 3$  s. The whole step response is shown in (a) with a zoom-in on the disturbance in (b).

## 4.4 Integral Resonance Control

The IRC's design procedure presented in 3.2 was carried out in continuous time, but each block in the scheme was individually discretized for the sake of comparison with the present controller. The identified discrete system in (2.3) was converted to continuous time with the zero-order hold method in Matlab resulting in a continuous time transfer function with six zeros and seven poles. Since the system has a relative degree of one, the negative feedforward will introduce one additional zero. As seen in the pole-zero plot comparison in Figure 4.12, a feedforward of  $D_f = -1.2$  was sufficient to introduce one zero and place it and its complex conjugate below the first resonance frequency. This and the zero-pole interlacing for the higher order modes can be seen in Figure 4.12b, where the zoom-in shows the complex conjugate zeros below the first resonance mode.

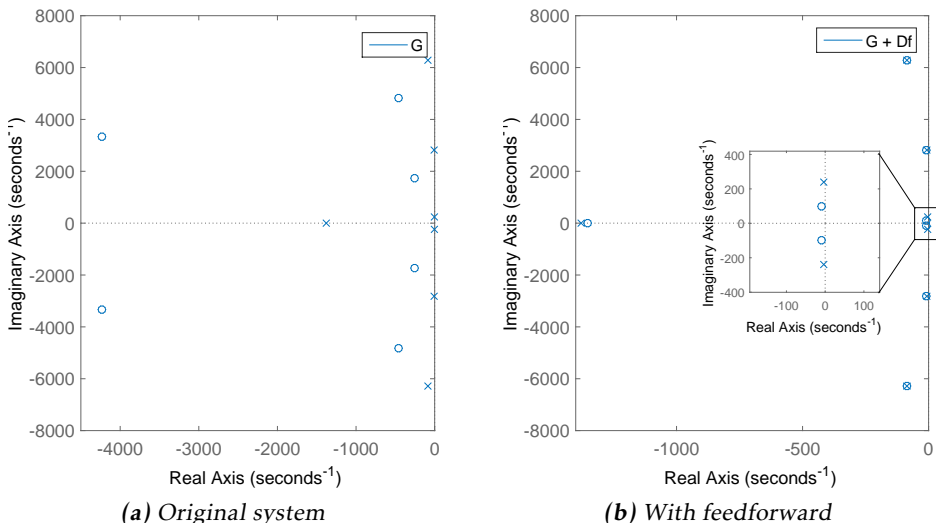


**Figure 4.12:** Comparison of pole-zero plot before and after the addition of the negative feedforward. After adding the feedforward to the system, which poles and zeros are shown in (a), the zeros and poles are interlacing as seen in (b).

The corresponding Bode plot can be seen in Figure 4.13, showing the complex conjugate pair of zeros as a dip before the first resonance peak.

The integral controller  $C(s) = -k/s$  was added according to Section 3.2 and a gain of  $k = 314$  was found to maximize the damping, by using the root locus technique. The open and closed loop system of the IRC damping loop depicted in Figure 3.2 is shown in Figure 4.14. It is clear that the integral controller damps out the first resonance peak efficiently in closed loop.

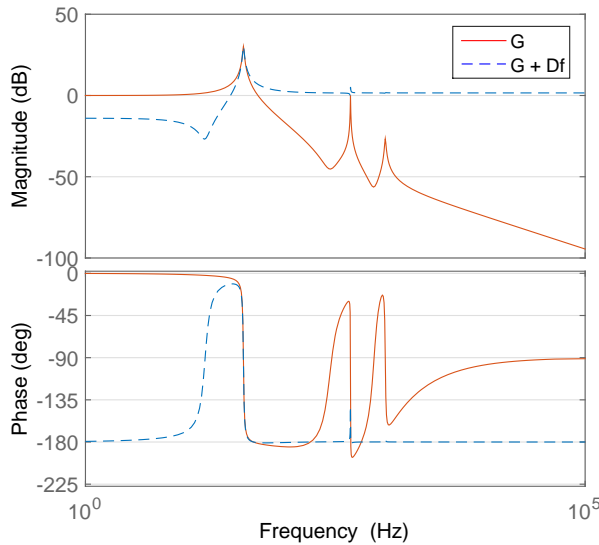


**Figure 4.13:** Bode plot of the continues time system before and after the addition of the negative feedforward.

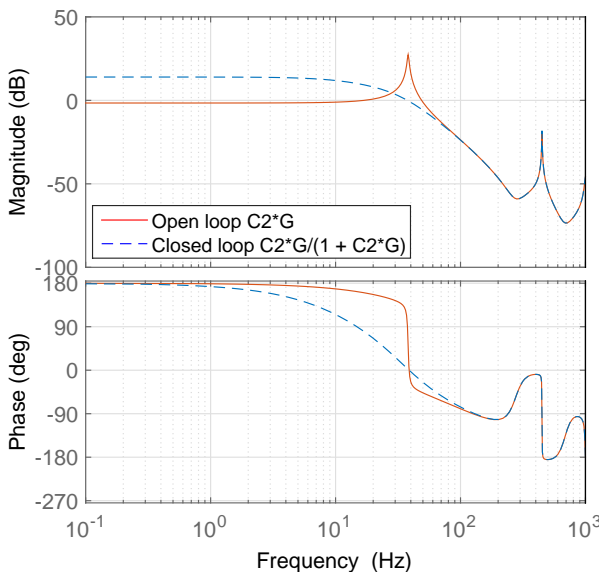


**Figure 4.14:** Bode plot of the discretized open and closed loop of the IRC damping loop i.e. the inner loop of the total control loop depicted in Figure 3.2.

Finally, the damped system was enclosed in an outer loop with a second controller  $C_1(z)$  for reference tracking capability.  $C_1(z)$  was designed to be robust to model errors i.e. keep the sensitivity function stated in (3.17b) low for the frequencies that the model changes with. It was also designed to attenuate higher order resonances by including a notch filter.  $C_1(z)$  was designed in Matlab's SISO-Tool and is presented in (4.2).

$$C_1(z) = \frac{-13.54z^5 + 40.92z^4 - 57.47z^3 + 55.89z^2 - 35.87z + 10.05}{z^5 - 1.65z^4 + 0.80z^3 - 0.16z^2 + 0.014z - 0.00042} \quad (4.2)$$

The resulting closed loop system and the sensitivity function is shown in Figure 4.15 and 4.16, respectively. The plots show that the use of the IRC has increased the closed loop bandwidth from 11 Hz to 73 Hz. The IRC's sensitivity function also shows that the IRC scheme attenuates disturbances better in the low frequency range and in the region within 24-64 Hz. The sensitivity function is written in Section 3.2.

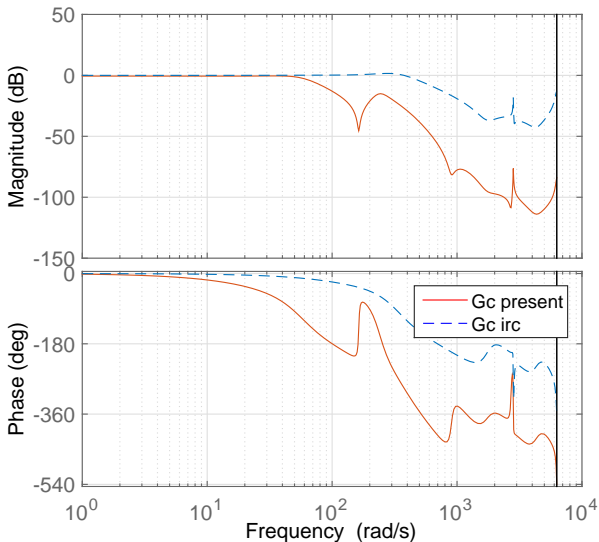


**Figure 4.15:** Bode plot of the discretized closed loop system of the outer control loop for the IRC depicted in Figure 3.3 and the present closed loop system.

The IRC's tracking performance is shown in Figure 4.17 where the tracking error has been considerably reduced owing to the high bandwidth of the IRC.

The robustness test performed for the adaptive controller was done for the IRC controller accordingly. Figure 4.18a shows the periodic response and its tracking error when the model is changed linearly according to Figure 4.8b. The IRC handles the model drift better than the present controller.

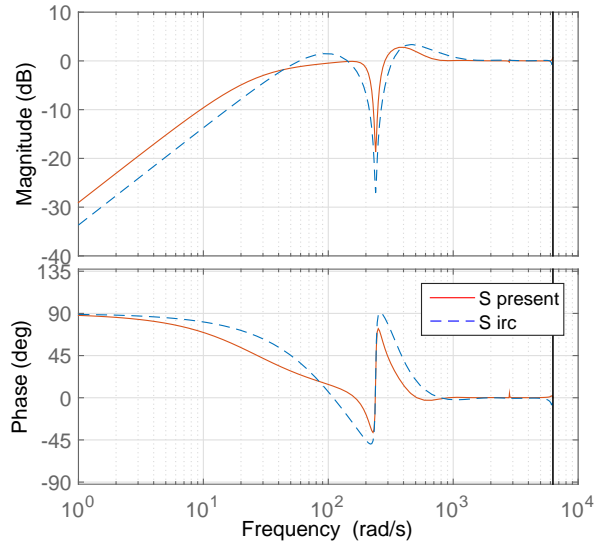


**Figure 4.16:** Sensitivity function of the IRC and the present control approach.

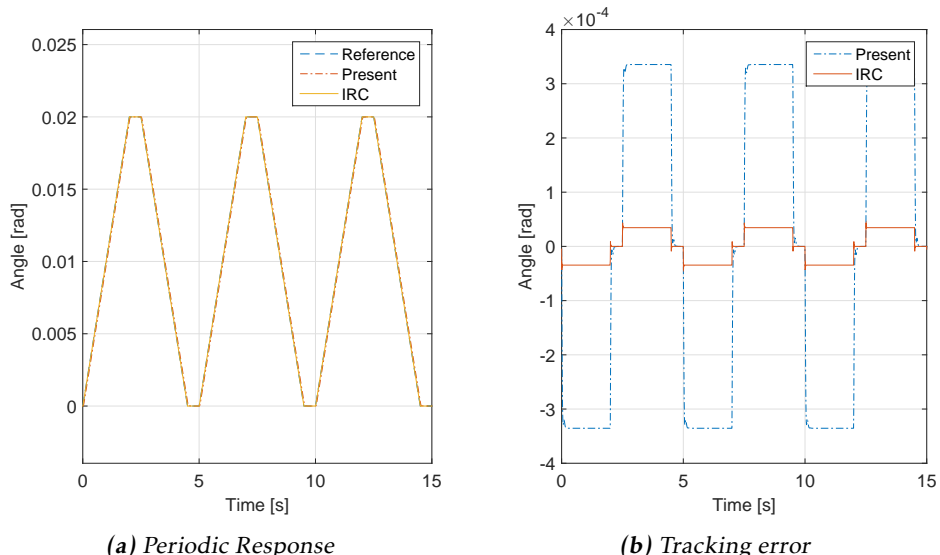
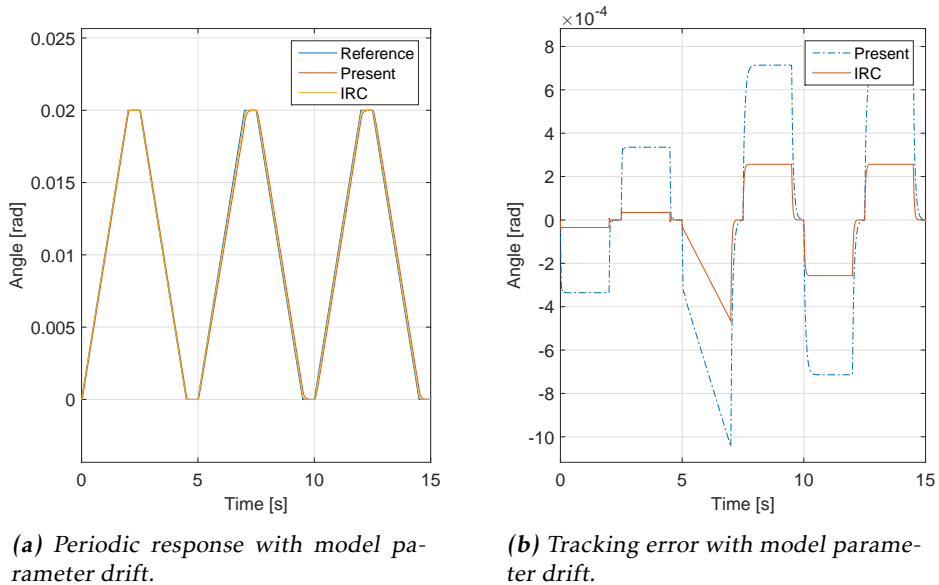


**Figure 4.17:** Periodical input response of the IRC and the present controller shown in (a) with the tracking error shown in (b).



(a) Periodic response with model parameter drift.

(b) Tracking error with model parameter drift.

**Figure 4.18:** Periodical input response with induced model errors for the IRC and the present controller. The model error is increased linearly from  $t = 5$  s to  $t = 7$  s. The resulting responses are shown in (a) with the tracking error is shown in (b).

The capability of rejecting disturbances on the input signal is shown in Figure 4.19. As seen in the zoom-in, the IRC is slightly more damped but has a high frequency ringing in 448Hz, the same frequency as the model's second resonance peak. This ringing is also showing in the present controller but is less dominant.

The capability of rejecting disturbances on the output signal is shown in Figure 4.20. Since the impulse is added directly on the output the step response peaks accordingly at  $t = 3$  s. It is hard to tell from Figure 4.20b, but the peak is visible for both of the control approaches. After the peak, the methods perform similarly but with a higher damping of the low frequency mode for the IRC oscillations as shown in the zoom-in.

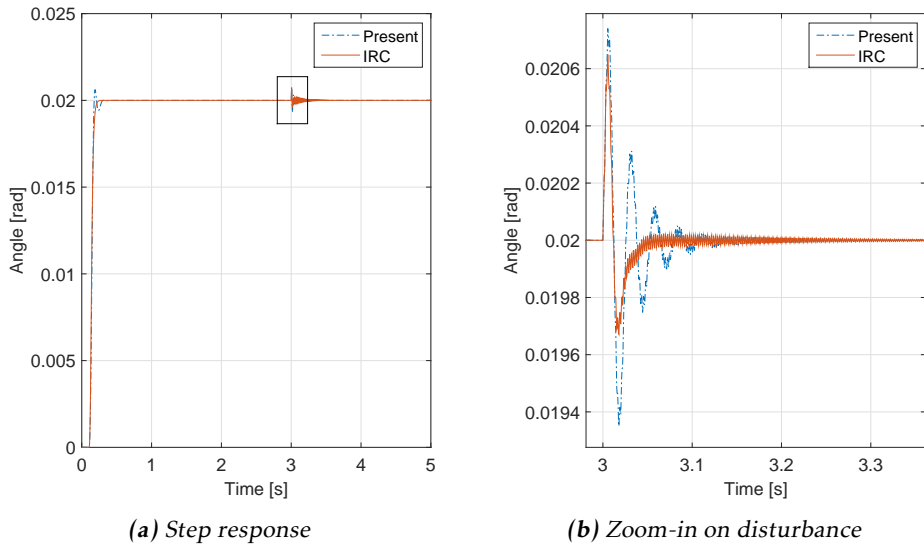


**Figure 4.19:** Step response with a disturbance impulse (amplitude of 5.1 mV) added to the input of the system at  $t = 3$  s. The whole step response is shown in (a) with a zoom-in on the disturbance in (b).

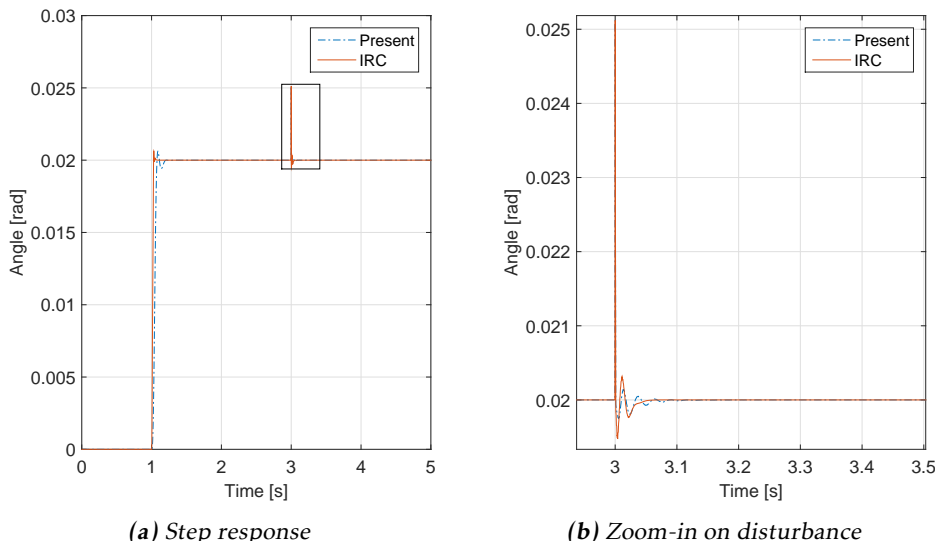


**Figure 4.20:** Step response with a disturbance impulse (amplitude of 5.1 mrad) added to the output of the system at  $t = 3$  s. The whole step response is shown in (a) with a zoom-in on the disturbance in (b).

To further verify the capability of handling disturbances with various frequencies, a white noise was applied to the input and output of the system, illustrated in Figure 3.3 as  $d_i$  and  $d_o$ , respectively. The FFT was then performed on the output ( $y$ ) to verify the disturbance rejection for all frequencies, and the result is presented in Figure 4.21 and Figure 4.22.

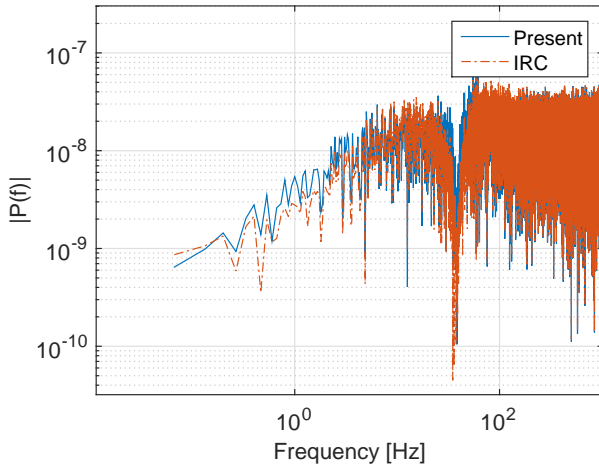


**Figure 4.21:** The FFT of the output signal from the IRC and the present closed loop system when applying white noise to the output of the system.

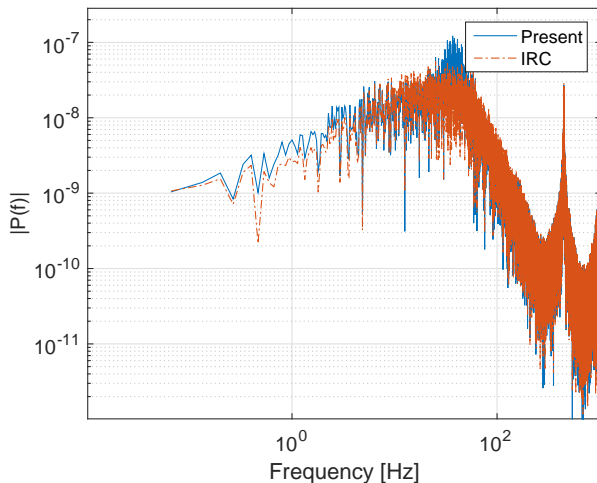


**Figure 4.22:** The FFT of the output signal from the IRC and the present closed loop system when applying white noise to the input of the system.

The standard deviations of the output signal with a disturbance with  $\sigma = 1.41 \mu\text{rad}$  added to both the output and input for the IRC and the present approach are summarized in Table 4.2.

| Disturbance applied to:             | input | output |
|-------------------------------------|-------|--------|
| $\sigma_{IRC}/\sigma_{Present}$ [%] | 66    | 102    |

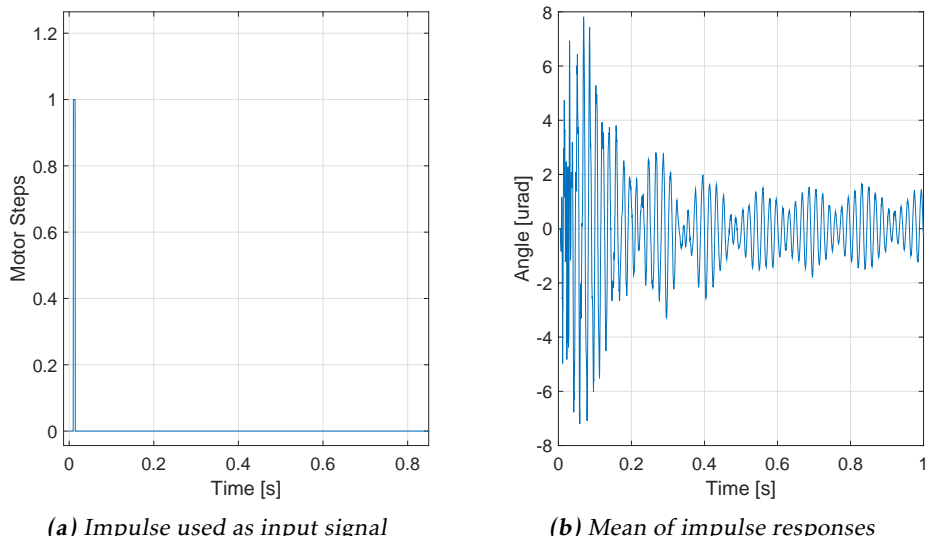
**Table 4.2:** Standard deviations of the output signal with white noise added as a disturbance on the output of the system

## 4.5 Harmonic Cancellation

All harmonic cancellation methods were implemented and benchmarked with realistic disturbance data acquired with the lab setup described in Section 5.1. The disturbance data was acquired in open loop during a linear axis movement around the operating point of the linear axis, which is 3 mm out from the inner position with respect to the beam. Each cancellation method was benchmarked individually with respect to cancellation performance and robustness to model errors.

### 4.5.1 Feedforward Disturbance Cancellation

The FDC methodology cancels out known disturbances coming from a linear axis movement. The stepping signal sent to the motor is known at all time and is therefore suitable to be used as input signal ( $d_0$  in Figure 3.4) to the disturbance model. Data was acquired in open loop during a linear axis movement corresponding to 50 steps of the stepping motor. The movement was performed with four different speeds (1, 2, 5 and 10 steps/s) around the operating point. The chosen linear speeds were relatively low compared to normal operation, but used for the purpose of getting enough time between each step in order for the response to have sufficient time to settle. Figure 4.23 shows the yaw angle response from one motor step and the impulse used for the identification of the disturbance model.



*(a) Impulse used as input signal      (b) Mean of impulse responses*

**Figure 4.23:** Input signal (a) and step response (b) used for modeling the disturbance. The step response was calculated by taking the mean of 50 time-synchronized acquired step responses at a movement of 1 step/s.

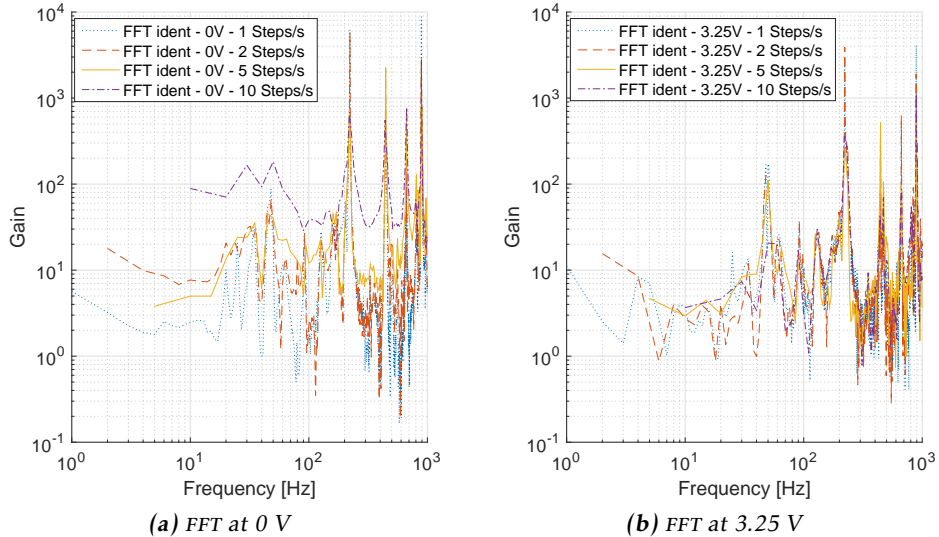


**Figure 4.24:** Disturbance representation in the frequency domain. The plot shows the calculated FFT at two different positions,  $0\text{ V} \sim -10\text{ mrad}$  (a) and  $3.25\text{ V} \sim 0\text{ mrad}$  (b) for the speeds 1,2,5 and 10 steps/s.

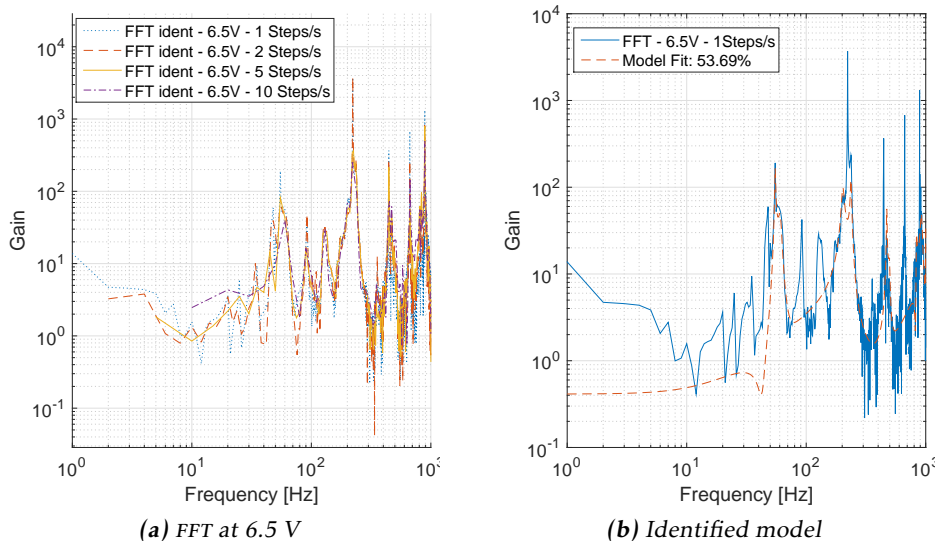
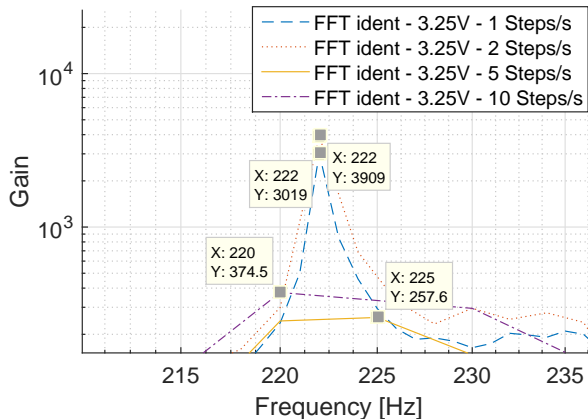


**Figure 4.25:** Disturbance representation in the frequency domain with the identified model. The calculated FFT at  $6.5\text{ V} \sim 10\text{ mrad}$  is shown in (a) and the identified model to the mean of the data in (a) is shown in (b).

In a real implementation, the stepping voltage would be used to form a pulse train containing impulses similar to the one showed in Figure 4.23a.

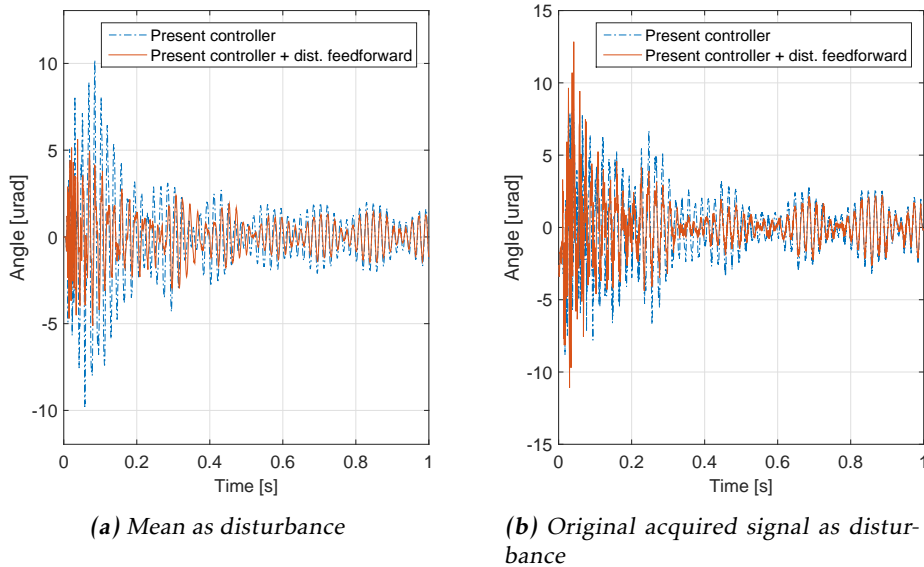
The empirical estimate of the disturbance model  $P_d$  is obtained by dividing the FFT of (b) with the FFT of (a) in Figure 4.23. The resulting empirical estimate is shown for different positions and speeds in Figure 4.24 and 4.25a . As seen in the figures, there are distinct peaks at around 220, 445, 670 and 890 Hz. The amplitude and the frequency of the resonance peaks are varying with the step rate as seen in Figure 4.26.

Figure 4.25 shows the identified model for the data acquired at 6.5 V and 1 step/s. This data was chosen due to its homogeneous shape at different step rates. In order to sufficiently model four resonances, a 19 zeros and 20 poles transfer function was needed. The model was used in the simulations but has to be reduced for a reasonable implementation in terms of computational efficiency. The identification was performed using Matlab System Identification Toolbox with a selected frequency focus from 30-1000 Hz, to avoid modeling low frequency components below the first resonance peak. The identified disturbance model  $P_d(z)$  is presented in its final form in Appendix A.2.  $K_f(z)$  was calculated as  $K_f(z) = P_d(z)/G(z)$ .



**Figure 4.26:** Zoom-in on the first resonance peak of the FFT performed on the data acquired at 3.25 V  $\sim$  0 mrad. The top peak of the resonance is varying with the step rate i.e. 5 step/s  $\sim$  225 Hz and 10 step/s  $\sim$  220 Hz.

The disturbance model was benchmarked with two slightly different disturbances, first with the mean shown in Figure 4.23b (the signal used in the identification) and then with a signal picked out as one period from the original acquired data. The cancellation performance at 6.5 V and 1 step/s can be seen in Figure 4.27. The FDC manages to mitigate the disturbance on the yaw angle by almost half of the amplitude with the mean fed as disturbance. With the more realistic disturbance in (b) the disturbance cancellation is however less effective.



**Figure 4.27:** Feedforward disturbance cancellation with the mean of the acquired response added as disturbance (a) and one period of the acquired response added as disturbance (b). The disturbance cancellation is less effective with a slightly different disturbance.

To illustrate the model efficiency with different step rates, a benchmarking test with the same identified model as above was performed with the mean corresponding to each of the stepping rates added as disturbance. The outcome is presented in Table 4.3 as the standard deviation of the yaw angle, showing that a single model is sufficient to reduce the disturbance level for several other stepping rates as well.

| Speed                             | 1 step/s | 2 step/s | 5 step/s | 10 step/s |
|-----------------------------------|----------|----------|----------|-----------|
| $\sigma_{Present}$ [urad]         | 2.15     | 2.23     | 3.90     | 3.76      |
| $\sigma_{Present+dist.FF}$ [urad] | 1.19     | 2.04     | 2.06     | 2.59      |

**Table 4.3:** Standard deviations of the output with and without disturbance feedforward for the different speeds with the mean of the acquired response corresponding to each speed added as disturbance. The model used in the disturbance feedforward was identified from the 6.5 V and 1 step/s data.

To benchmark how well the cancellation works with model errors, a simulation with four different perturbed models was performed with the disturbance feedforward based on the same models as before. The models including the original system itself is shown in Figure 4.28, where the first resonance peak has been

perturbed. This models the previously identified behavior when the rotational stage rotates from -10 to 10 mrad.

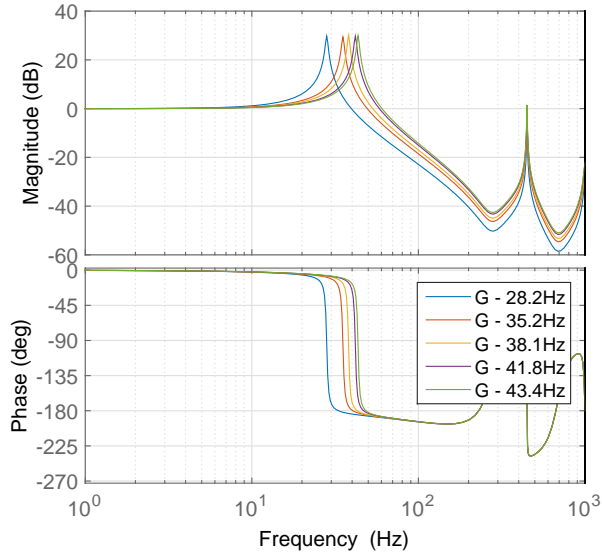


**Figure 4.28:** Bode plot of the five different models used for the simulation of model error, including the original model  $G - 38.1\text{Hz}$ .

The FFT of the simulation results can be seen in Figure 4.29a where the attenuation of the major disturbance component is shown. The simulations indicate that the cancellation is still efficient even with model errors being present. The original controller and system without disturbance cancellation is included in the plots as a reference and is named  $G - 38.1\text{ Hz}$ . Figure 4.29b illustrates the impact that the model errors have on the attenuation of some other resonances present in the system. Here 92.3 Hz is chosen as an example to illustrate that the cancellation with model errors can lead to amplification at some frequencies.

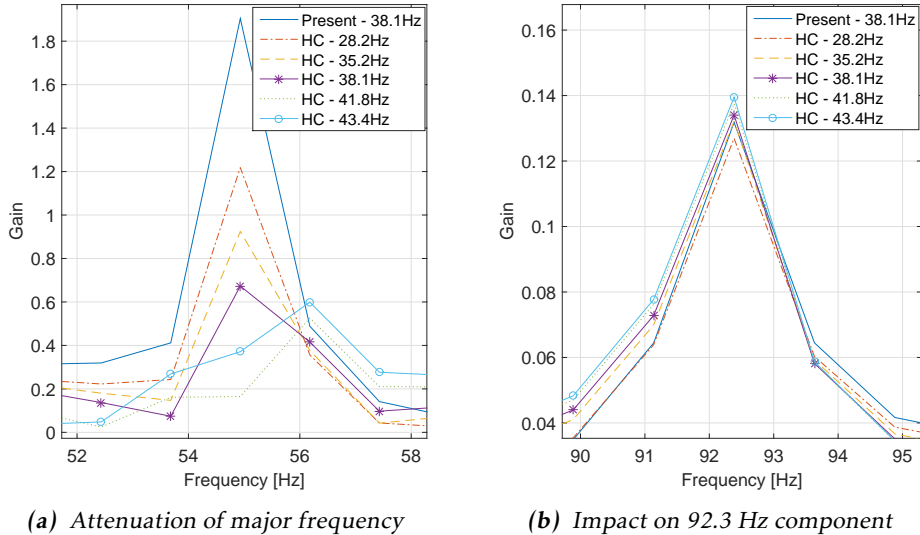


**Figure 4.29:** Disturbance cancellation effectiveness with model errors. The attenuation of the major frequency is shown in (a) while the attenuation of the 92.3 Hz component is shown in (b).

### 4.5.2 Cancellation with Internal Model Principle

The implementation of the IMP cancellation method was based on the theory in Section 3.3.2. A pure sinusoidal disturbance was used as the generating polynomial  $\Gamma(s) = s^2 + \omega^2$ , where the angular frequency to reject was chosen to  $\omega = 100\pi$  rad/s. This choice of polynomial gives full attenuation in the selected frequency but impacts on the attenuation of system's first resonance peak at 38.1 Hz. Hence, in order to get sufficient attenuation at both of the frequencies, a bit of damping was added to the polynomial. The normalized continuous time transfer function that was discretized and added to the system is presented below.

$$C_{imp}(s) = \frac{(100\pi)^2}{s^2 + s + (100\pi)^2} \quad (4.3)$$

The controller, shown in its full in (4.4), was tuned in Matlab's SISO-tool with the goal to achieve equivalent performance as the present controller. The controller was based on a PI-controller with a notch filter to damp out higher order frequency modes and a complex pair of zeros placed between the two resonance peaks at 38.1 and 50 Hz to gain phase margin. Finally, a lead-filter was added to increase the phase margin even further.

$$C(z) = \frac{25.33z^7 - 130.6z^6 + 301.9z^5 - 429z^4 + 424.7z^3 - 291.5z^2 + 121.8z - 22.64}{z^7 - 3.6z^6 + 5.4z^5 - 4.5z^4 + 2.2z^3 - 0.63z^2 + 0.096z - 0.0061} \quad (4.4)$$

Figure 4.30 shows the resulting closed loop system and the sensitivity function from output disturbance to system output. The two notches at 38.1 and 50 Hz are clearly visible in the sensitivity function. Note that the attenuation at 38.1 Hz is now slightly reduced for the IMP approach. This phenomenon is explained by Bode's integral constraints [13] meaning that if the sensitivity function is decreased in one frequency region it will increase at another.

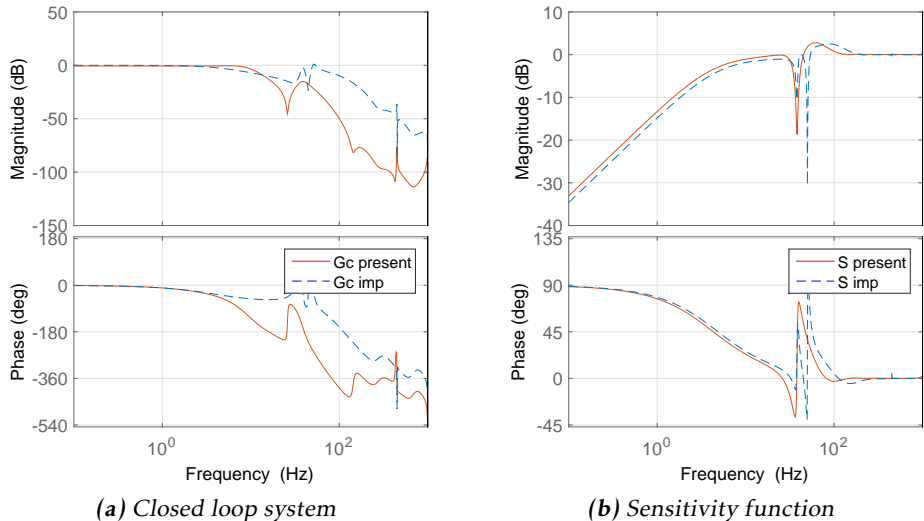


**Figure 4.30:** Bode plot of the closed loop system shown in (a) and the sensitivity function (from output disturbance to system output) shown in (b) of the IMP and the present controller. The IMP is now attenuating disturbances at 50 Hz as seen in (b).

The IMP method was benchmarked against the present controller in all tests. As a proof of concept, a 50 Hz sinusoidal with an amplitude of 0.01  $\mu$ rad was added as a disturbance and the attenuation (in the perfect case) can be seen in Figure 4.31. The IMP managed to attenuate 96% of the added disturbance. The remaining 4% can be explained by the damping that was added to the generating polynomial.

For a more realistic benchmarking, disturbance data collected at 10 steps/s was added to the output of the system. The result is presented in Figure 4.32 where it is clear that the 50 Hz component has been damped out efficiently.

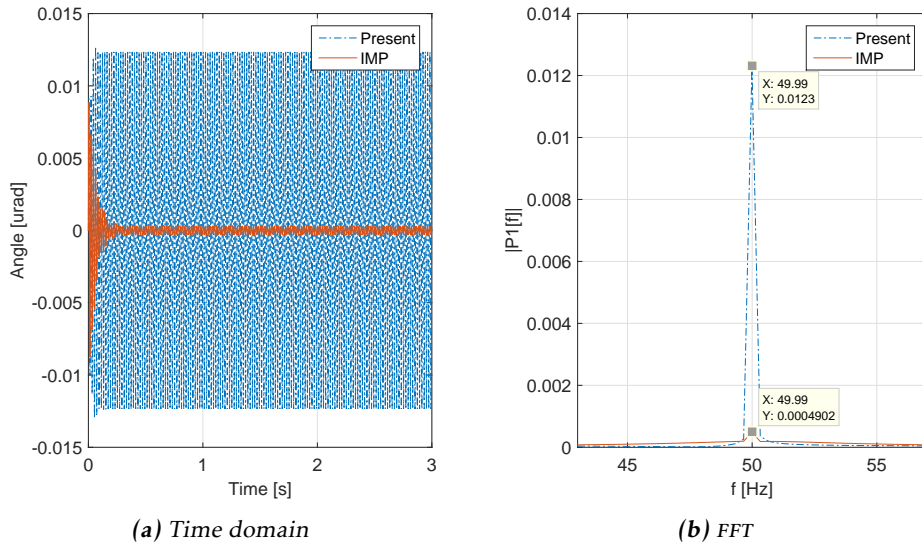


**Figure 4.31:** Closed loop time response with 50 Hz disturbance added to the output of the system. The cancellation of the 50 Hz component can both be seen in the time domain (a) and in the FFT (b). The FFT was performed after the response had settled.

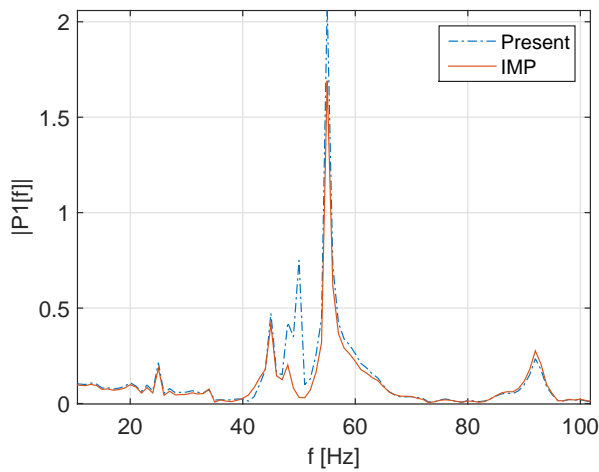


**Figure 4.32:** Cancellation of the 50 Hz component with the real acquired disturbance added to the output of the system. The FFT was performed after cancellation had settled.

Finally, the cancellation approach was tested for model robustness following the procedure described in Section 4.5.1. The perturbed models used in the simulation can be seen in Figure 4.28. The attenuation of the selected frequency is presented in Figure 4.33a showing that the cancellation is efficient for major model errors. One main drawback with this approach is depicted in Figure 4.33b where the 130 Hz component has been amplified due to the addition of the IMP cancellation strategy.

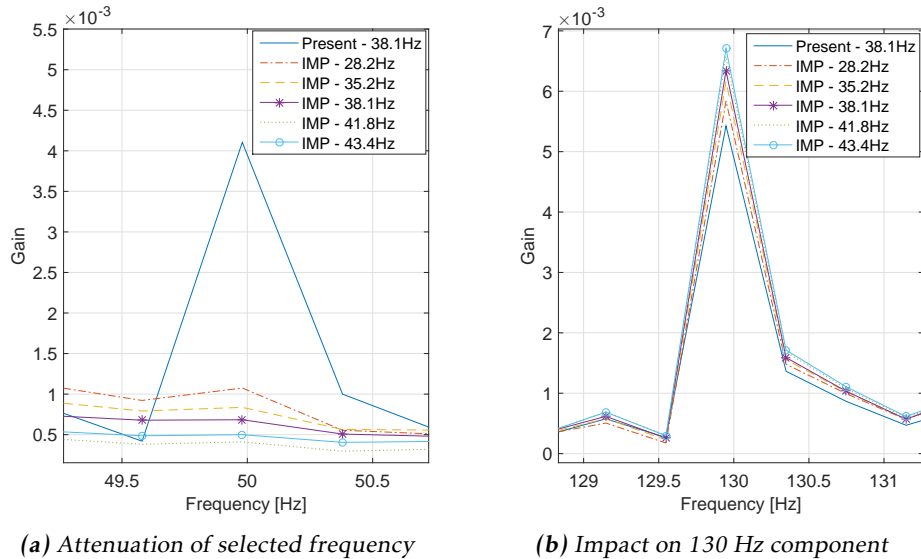


**Figure 4.33:** Disturbance cancellation effectiveness with model errors. The attenuation of the major frequency is shown in (a) and the unwanted attenuation of the 130 Hz component is shown in (b).

### 4.5.3 Repetitive Feedforward Disturbance Cancellation

The Repetitive Feedforward Disturbance Cancellation (RFDC) method was implemented to reject three known disturbances. Hence, three second order disturbance models as given in (3.26) were augmented as shown in (4.5). The chosen angular frequencies for cancellation were  $w_1 = 120\pi$ ,  $w_2 = 180\pi$  and  $w_3 = 400\pi$  rad/s.

$$\mathbf{A}_{de} = \text{diag}\left(\begin{bmatrix} 0 & 1 \\ -w_1^2 & 0 \end{bmatrix}, \begin{bmatrix} 0 & 1 \\ -w_2^2 & 0 \end{bmatrix}, \begin{bmatrix} 0 & 1 \\ -w_3^2 & 0 \end{bmatrix}\right) \quad (4.5a)$$

$$\mathbf{C}_{de} = \begin{bmatrix} 1 & 0 & 1 & 0 & 1 & 0 \end{bmatrix} \quad (4.5b)$$

These equations were augmented according to (3.30) with the discrete time system matrices which can be seen in its full form in Appendix A.1. The observer was implemented in state space form, with the following equations.

$$\mathbf{A}_{obs} = \mathbf{A} - \mathbf{K}\mathbf{C} \quad (4.6a)$$

$$\mathbf{B}_{obs} = [\mathbf{B}, \mathbf{K}]^T \quad (4.6b)$$

$$\mathbf{C}_{obs} = \text{diag}(\mathbf{C}_{zs}, \mathbf{C}_{zd}, \mathbf{C}_{zd}, \mathbf{C}_{zd}) \quad (4.6c)$$

$$\mathbf{D}_{obs} = \text{zeros}(4, 2) \quad (4.6d)$$

The observer gain  $\mathbf{K}$  was calculated using Kalman theory (`d1qe` in Matlab), with a high measurement ( $\mathbf{R}$ ) to process noise ( $\mathbf{Q}$ ) ratio, trusting in the predefined model. The values provided to the `d1qe` function are listed in 4.4.

| Parameter | Value                                      |
|-----------|--|
| $R$       | 1  |
| $Q$       | $10^{-5}$                                  |
| $G$       | $[1, 0, 0, 0, 0, 0, 10, 0, 8, 0, 70, 0]^T$ |

**Table 4.4:** Parameters used for calculating the observer gain.

The RFDC method was benchmarked against the present controller in all tests. As a proof of concept, three sinusoidal disturbances with frequencies  $w_1$ ,  $w_2$  and  $w_3$  were added to the output of the system. Even though all of them were observed only  $w_3$  was used to cancel out the 200 Hz component to begin with. The result is shown in Figure 4.34, where it is clear that the 200 Hz disturbance is perfectly canceled by the feedforward algorithm. Since 200 Hz is a multiple of the sampling frequency  $F_s = 2000$  Hz, one period is sufficient to capture a full number of periods within the switching times. The switch was set to turn on (load one period) at  $t_{on} = 2$  s and to turn off at  $t_{off} = 2 + 1/200$  s, which was the time when all observed states had converged.

To prove the concept for multiple harmonic cancellation, all three of the estimated disturbances were added and subtracted from the input. To capture an

even number of cycles, the switching times for the 60 Hz and 90 Hz were set to [ $t_{on} = 2$  s,  $t_{off} = 2 + 6/60$  s] and [ $t_{on} = 2$  s,  $t_{off} = 2 + 9/90$  s], respectively.

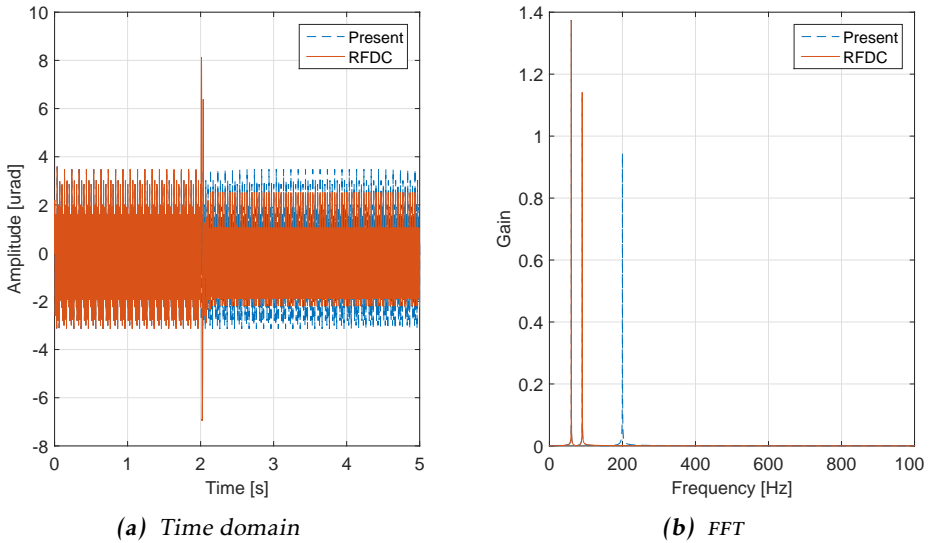


**Figure 4.34:** Closed loop response with a 60, 90 and a 200 Hz disturbance added to the output. The cancellation of the 200 Hz component can be seen in the time domain in (a). The FFT in (b) is performed on (a) after  $t = 2.5$  s.

The result is presented in Figure 4.35, which also illustrates a perfect cancellation. Note that the FFT analysis is performed on data from  $t=2.5$  to  $t=5$  s, i.e. at the time after the response from the feedforward cancellation had settled.

For a more realistic benchmarking, disturbance data collected at 10 steps/s was added to the output of the system.  $w_1$ ,  $w_2$  and  $w_3$  are all major components of the acquired disturbance so the observer model was kept the same as before. The result presented in linear scale is shown in Figure 4.36 where the modeled frequencies have been damped out efficiently. The gain of the 60Hz component for instance, is with the RFDC reduced by approximately 90% of its original amplitude.

As seen in Figure 4.36, the attenuation of the 200Hz is far from perfect. This is due to the higher noise level that now is present with the more realistic disturbance signal. A lower gain would reduce the noise in the observed disturbance, but would also lead to a longer convergence time. Figure 4.37 shows the FFT of the observed disturbance with a low gain and a settling time longer than 5 seconds. Figure 4.38 shows a less clean representation of the disturbance, achieved with a higher gain and a shorter settling time around 3 seconds.

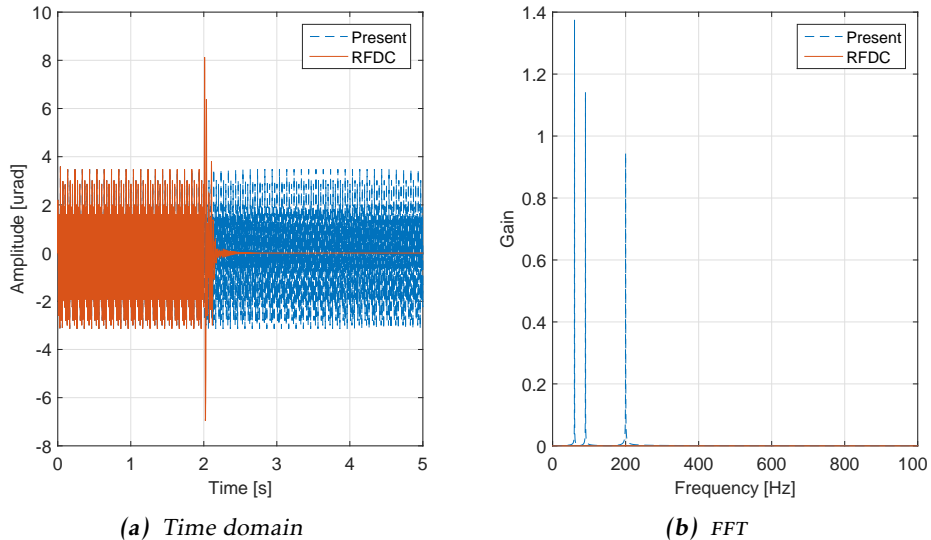


**Figure 4.35:** Multiple harmonic cancellation with disturbances added to the output. The cancellation of the 60, 90 and the 200 Hz component can be seen in the time domain in (a). The FFT in (b) is performed on (a) after  $t = 2.5$  s.

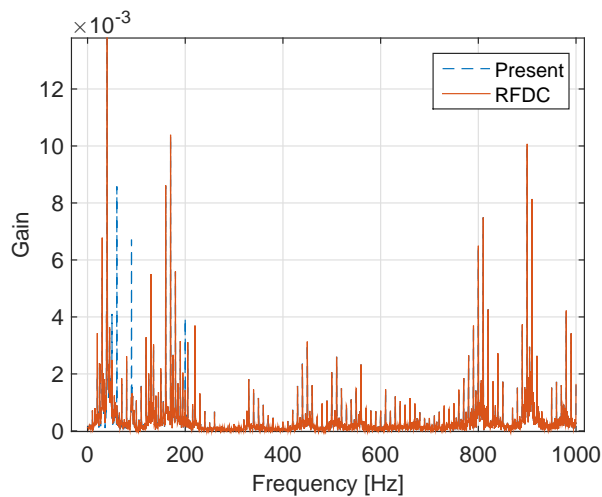


**Figure 4.36:** Multiple harmonic cancellation with real acquired disturbances added to the output of the system. The figure shows the FFT with and without the RFDC active. When it is active, it attenuates the 60, 90 and the 200 Hz component efficiently. The FFT was performed after the cancellation had settled.

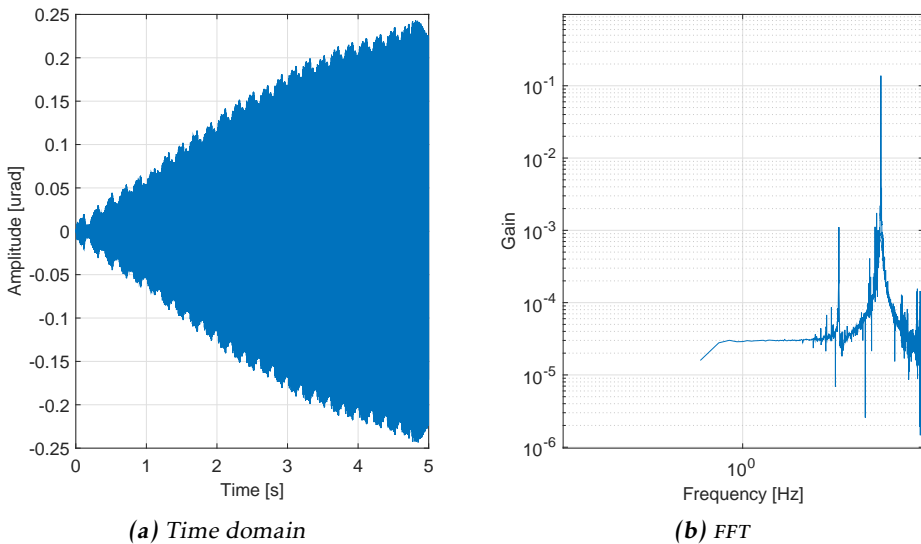


**Figure 4.37:** Observer convergence of the 200Hz harmonic with low gain,  $G = [1, 0, 0, 0, 0, 0, 10, 0, 8, 0, 10, 0]^T$ . The FFT of the time domain convergence (a) is presented in (b) which shows a good model of the 200 Hz harmonic.

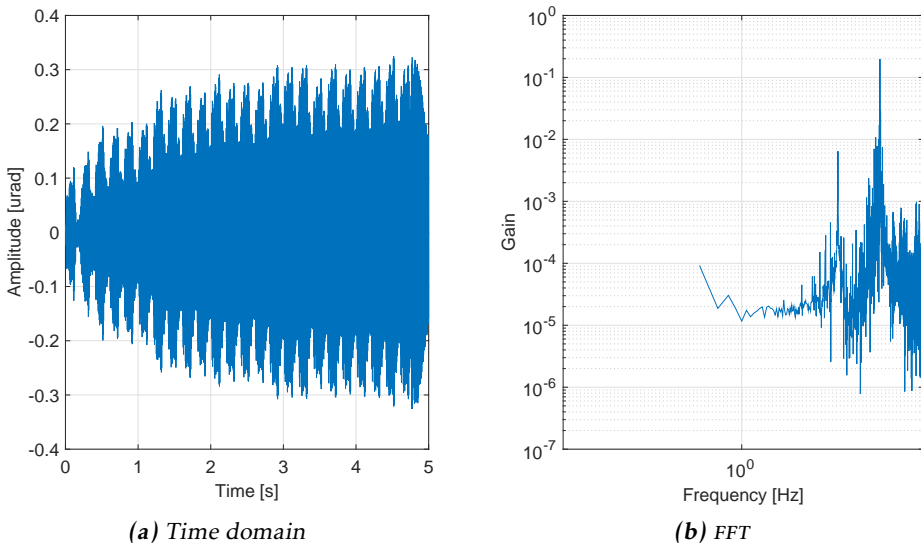


**Figure 4.38:** Observer convergence of the 200Hz harmonic with high gain,  $G = [1, 0, 0, 0, 0, 0, 10, 0, 8, 0, 70, 0]^T$ . The FFT of the time domain convergence (a) is presented in (b) which shows a less good model of the 200 Hz harmonic with a lot of other modeled frequency components in the region of 200 Hz.

An even higher gain would lead to more noise added to the model and a reduction in cancellation performance as illustrated in Figure 4.39. The figure shows that a shorter convergence time implies a reduction in cancellation performance. The figures show the cancellation of the 200Hz component with a convergence time of 2s in (a) achieved with a gain of 70 as before and a convergence time of 1s in (b) achieved with a gain of 140.

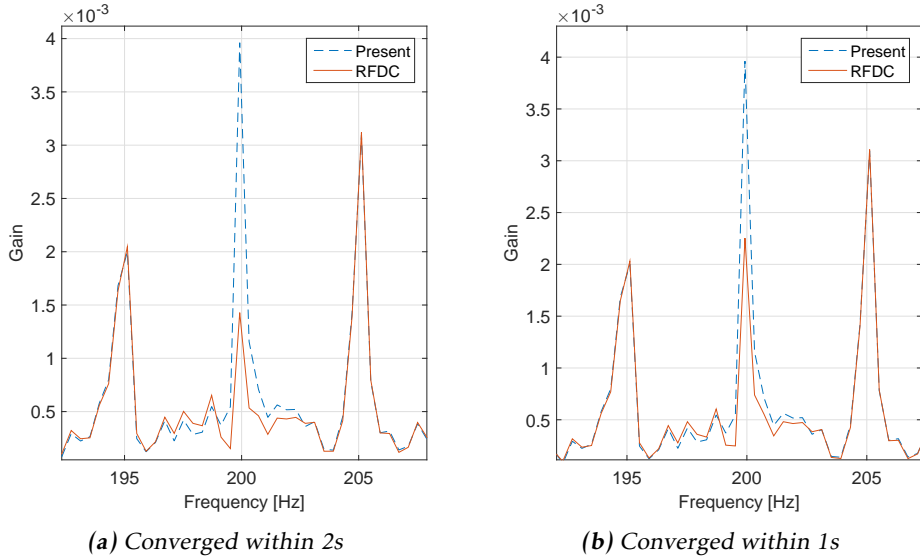


**Figure 4.39:** Cancellation effectiveness of the 200 Hz component with different converging times. The cancellation is more effective with a slower state convergence. The cancellation effectiveness with a state convergence of 2 s is shown in (a) and of 1 s in (b).

To overcome this issue, a bandpass filter could be added to reduce the noise level of the model and thereby enabling quicker convergence. The bandpass filter stated in (3.32) was used in the simulations with  $\omega = 400\pi$ ,  $k = 1/100$ ,  $\xi_a = 1$  and  $\xi_b = 0.01$ , which has zero phase shift for signals entering at 200Hz, but shifts all other frequencies. Tests were performed with this filter but without any increase in disturbance cancellation performance.

To benchmark the sensitivity to model errors, a similar simulation as in Section 4.5.1 was performed on the RFDC method. The perturbed models used in the simulation can be seen in Figure 4.28. The attenuation of the selected frequency is shown in Figure 4.40a showing that the cancellation is efficient with low model errors, but amplifies the component if the error is too large (RFDC-43.4 Hz in figure). Figure 4.40b illustrates that the RFDC is not amplifying other major frequencies components by showing one example e.g. the 130 Hz component.

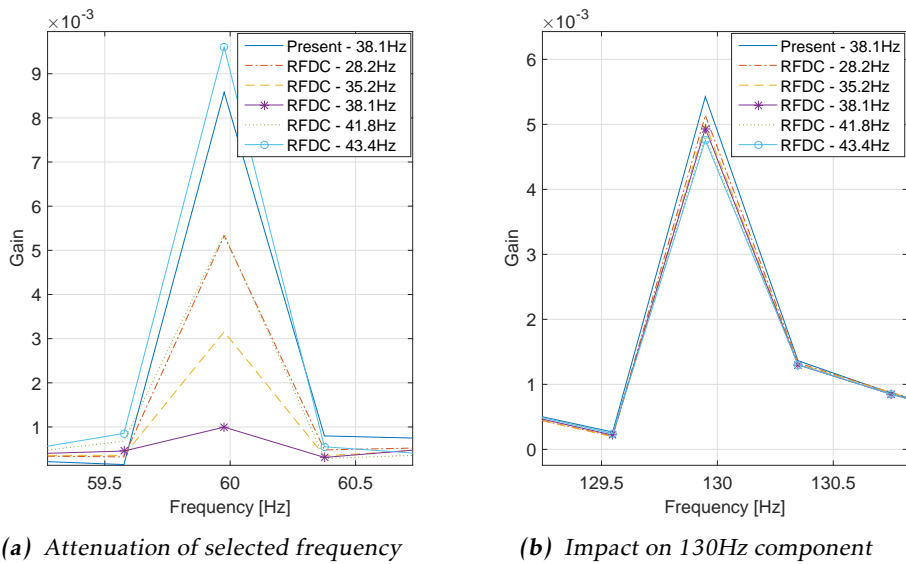


**Figure 4.40:** Disturbance cancellation effectiveness with model errors. The attenuation of the major frequency is shown in (a) and the unwanted attenuation of the 130 Hz component is shown in (b).

## 4.6 Comparison

This section compares and summarizes the different control methodologies. The IRC, MRACPE and the present controller are compared separately from the disturbance cancellation methodologies (FDC, RFDC and IMP). Table 4.5 and 4.6 summarizes comparable results presented in previous sections. Key values from the graphs have been collected to give the reader an overview of the achieved performance for each control approach.

In Table 4.5, the closed-loop bandwidth is presented for each approach, where "--" means that a theoretical bandwidth is missing for the MRACPE. The tracking error (row 3-7) is presented as the standard deviation of the difference between reference and output signal, acquired after each approach has settled. The tracking error with model errors being present is shown in row 4-7. Here, infinite tracking error means that the system is unstable. First resonance peak frequencies are selected to put the system on the border to instability. Row 7 presents the disturbance rejection with a disturbance added to the system output, measured in settling time from the time when the disturbance was added.

| No | Aspect  | Present  | IRC   | MRACPE   |
|----|---|--|---|--|
| 1  | Closed-loop Bandwidth [Hz]  | 9.7  | 73.3  | -  |
| 2  | Gain/Phase margin [dB / °]  | 14.4/66.2  | 13.1/49.4   | -  |
| 3  | Tracking error, periodic input $\sigma$ -[mrads]                                      | 0.29   | 0.03  | 0.11   |
| 4  | Tracking error with model errors (model's 1st resonance at 22.0Hz), $\sigma$ -[mrads] | $\infty$   | 0.03  | 0.21   |
| 5  | Tracking error with model errors (model's 1st resonance at 67.2Hz), $\sigma$ -[mrads] | $\infty$   | 0.03  | 0.11   |
| 6  | Tracking error with model errors (model's 1st resonance at 17.6Hz), $\sigma$ -[mrads] | $\infty$   | $\infty$  | 0.47   |
| 7  | Tracking error with model errors (model's 1st resonance at 77.7Hz), $\sigma$ -[mrads] | $\infty$   | $\infty$  | 0.11   |
| 8  | Output pulse disturbance rejection, settling time (1%) [ms]                           | 8  | 25  | 260  |
| 9  | Input/Output noise disturbance rejection, $\sigma$ -[ $\mu$ rad ]                     | 0.68/1.43  | 0.45/1.46   | 1.95/1.41  |
| 10 | Stability issues.   | Unstable with high model errors.                                   | Unstable with high model errors, but better than present. | Good adaption even with model errors, but tuning for quicker adaption easily leads to instability. Stability only proven in continuous time. |
| 11 | Design and implementation considerations.   | Straight-forward technique, allowing for basic stability analysis. | Same as present.  | Hard to tune. High computational burden for higher order models.   |

**Table 4.5:** Key parameters for the IRC, the MRACPE and the present control approach.

In Table 4.6, the cancellation effectiveness is measured as attenuation of the resonance peak with respect to the present approach. In row 3 and 4, the attenuation is measured with respect to the present controller that also includes the perturbed model written within the parentheses.

| No | Aspect  | FDC   | RFDC   | IMP  |
|----|---|---|--|--|
| 1  | Affecting closed loop system  | No  | No   | Yes  |
| 2  | Cancellation effectiveness of major frequency, attenuation-[%]                    | 64.6  | 88.4   | 83.3   |
| 3  | Cancellation with model errors (model's 1st resonance at 28.2Hz), attenuation-[%] | 40.5  | 26.6   | 73.5   |
| 4  | Cancellation with model errors (model's 1st resonance at 43.4Hz), attenuation-[%] | 57.7  | 5.0  | 83.4   |
| 5  | Implementation considerations.  | Requires high order model, computational demanding. | Requires observer, computational demanding. Can be used as add-on. | Controller must be retuned when selecting a new frequency. |

**Table 4.6:** Key parameters for the harmonic cancellation methodologies.

# 5

---

## Experimental Results

### 5.1 Setup

The results in Table 4.5 and 4.6 reveal, in terms of performance, stability and implementation considerations, two good candidates. The IRC as a stand-alone control approach and the RFDC as a harmonic cancellation add-on. Due to time limitations, only the RFDC was selected to be implemented in this thesis.

The experiments presented in this chapter has been conducted on the rotational stage described in Section 2.2. A National Instruments PXI was used to communicate with the goniometer and the rotational stage, responsible for acquisition and control. The PXI drives the rotational stage by applying a voltage between -1 and 7.5 V that passes through a linear amplifier with a gain of 20 resulting in an input signal ranging from -20 to 150 V. The analogue output has resolution of 10  $\mu$ V. The linear position was measured by a Linear Variable Differential Transformer (LVDT) and the resolver in the stepping motor giving a linear resolution of 5  $\mu$ m. The angle of the rotational head was measured by an interferometric system (shown in Figure 2.6) giving a theoretical angular resolution of 22 prad. During the acquisitions, the linear stage has been in its operating position (3 mm in from its inner position) and the rotational stage has been in 6.2 mrad or 6.5 V.

#### 5.1.1 Implementation

The control loop consisting of the original controller described in Section 2.5 was executed on the PXI with an updating frequency of 2 kHz. The RFDC was implemented using LabVIEW and added to the existing control loop. The graphical user interface (GUI) that was created to operate the cancellation is shown in Figure 5.1.

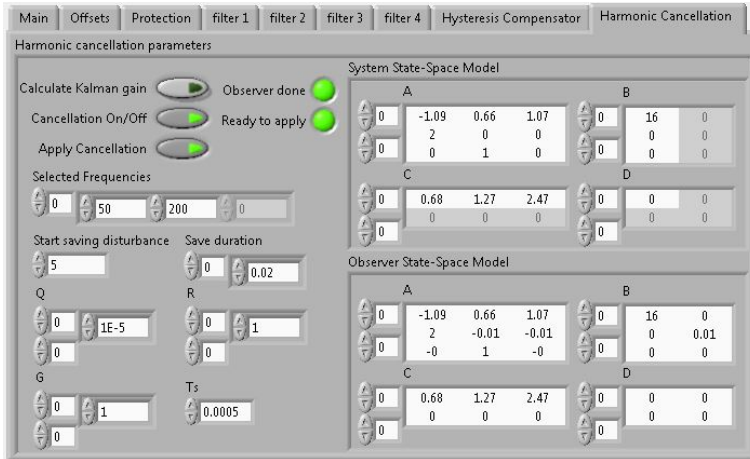


**Figure 5.1:** Graphical user interface of the RFDC implementation.

As seen in the GUI the method requires a system model, specification of the selected frequencies, a time after initialization when the observer shall start and how long it should observe. This time must, for efficient cancellation, be a multiple of the selected disturbance period time. In the initialization phase the observer model is calculated by pressing *Calculate Kalman gain*. The calculations are based on the system model and the specified tuning parameters. Cancellation is initialized by pressing the *Cancellation ON/OFF*, which starts the observation. *Observer done* indicates when the observation has finished and *Ready to apply* when the cancellation is ready to be applied.

## 5.2 Cancellation Verification

The cancellation effectiveness has been evaluated in a number of different benchmarking test both in open and closed loop. Single disturbance cancellation was benchmarked by canceling an artificial disturbance added to the system by a shaker. The shaker consist of a piezoelectric actuator mounted in a prestressed structure, which generates oscillations according to the applied AC voltage. Single disturbance cancellation was also benchmarked with real environmental harmonic disturbances that was not generated by the shaker. A small test with a disturbance created and inserted directly in the code was also done to show that the algorithm did not contain any phase shifting errors. Finally the approach was tested for cancellation of multiple frequency components simultaneously.

### 5.2.1 Single Disturbance

The RFDC was first evaluated in open loop with single harmonics generated by the shaker. In the first test the shaker was set to generate an 80 Hz disturbance

(amplitude set to 300 mV). Data was then acquired with and without the disturbance cancellation algorithm active and the result is presented in Figure 5.2 and Figure 5.3 which show the cancellation performance in time and frequency domain, respectively. Note that the acquisitions were taken successively and de-trended to mitigate the creep effect. As seen in the figures, the RFDC has reduced

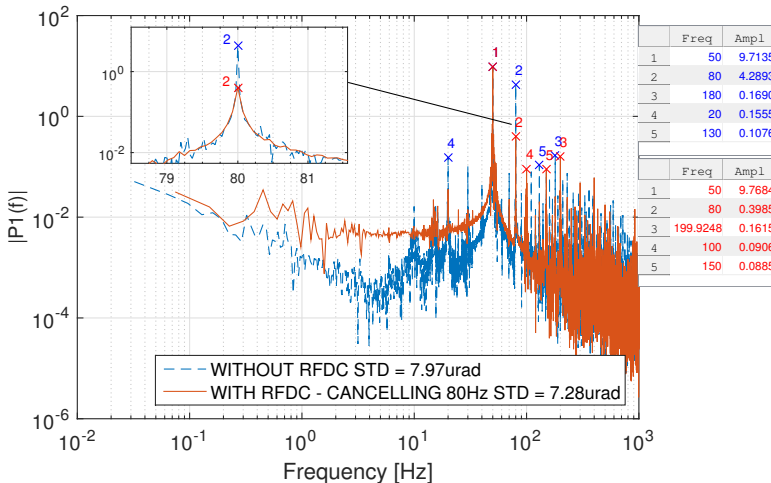


**Figure 5.2:** FFT of the yaw angle response acquired in open loop with and without the RFDC active. Cancellation of the 80 Hz component generated by the shaker. The table to the right of the figures shows the amplitude of the 5 highest resonance peaks displayed in descending order.

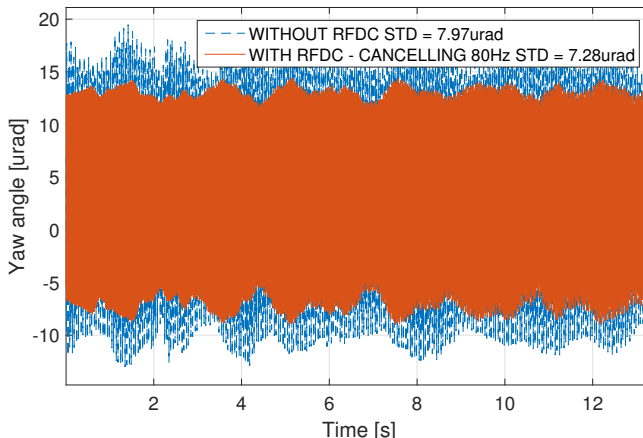


**Figure 5.3:** Open loop response showing the development of the yaw angle over time, with and without the RFDC active. Cancellation of the 80 Hz component generated by the shaker.

the 80 Hz component by 90% of its original amplitude. The standard deviation of the signal in Figure 5.3 was reduced by more than 8% due to the significance of the 80 Hz resonance peak.

Similar tests were performed with the controller in closed loop. The performance of the RFDC is shown in Figure 5.4, where the RFDC has reduced the 80 Hz component by 76% of its original amplitude.

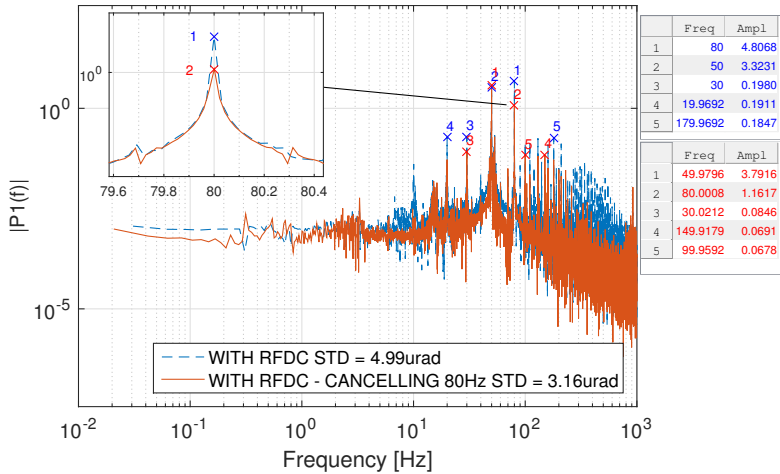


**Figure 5.4:** FFT of the yaw angle response acquired in closed loop with and without the RFDC active. Cancellation of the 80 Hz component generated by the shaker.

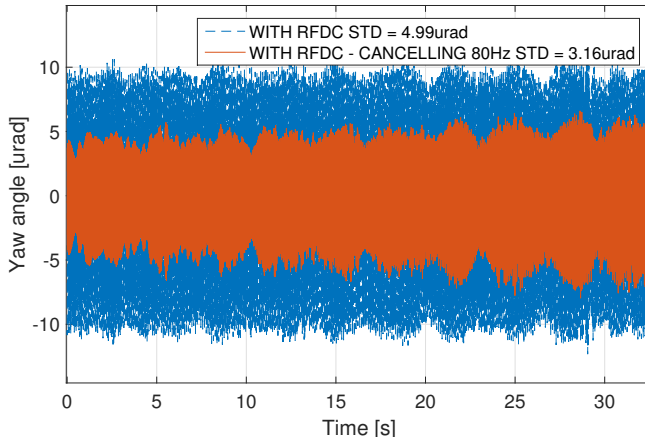


**Figure 5.5:** Closed loop response showing the development of the yaw angle over time, with and without the RFDC active. Cancellation of the 80 Hz component generated by the shaker.

Figure 5.4 also reveals a small inclination of the yaw angle evolving over time, i.e. the attenuation loses effect. In fact, looking over a larger period of time, the effect is oscillating. This effect is known as the "beat effect" and discussed further in Section 5.2.3. To further verify the performance, similar tests were also performed without the shaker applying an external disturbance. The selected disturbance was now identified by taking closed loop measurements to find dominating frequencies not attenuated by the controller itself. The 50 Hz was identified to be the most dominating component as shown in the series without the RFDC active in Figure 5.6. This frequency was selected and attenuated by the RFDC, resulting in a reduction of 51% of the 50 Hz component's original amplitude. The attenuation of the 50 Hz component improved the overall yaw angle accuracy as shown in Figure 5.7, where the activation transient is captured.

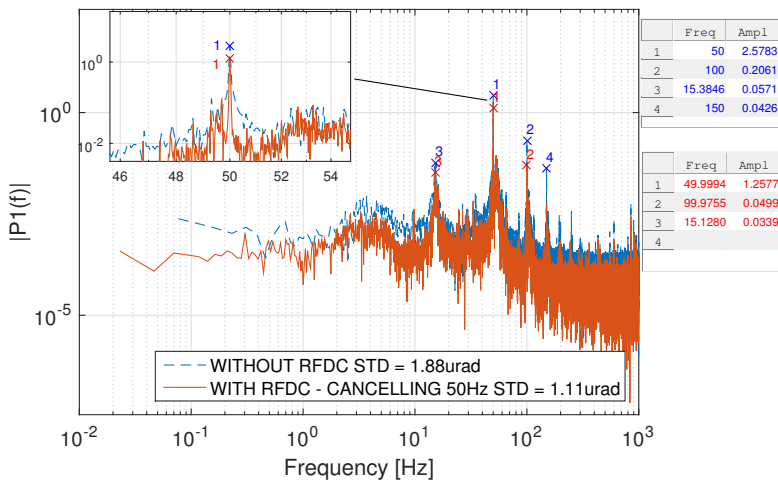


**Figure 5.6:** FFT of the yaw angle response acquired in closed loop with and without the RFDC active. Cancellation of the 50 Hz component originating from environmental disturbances.

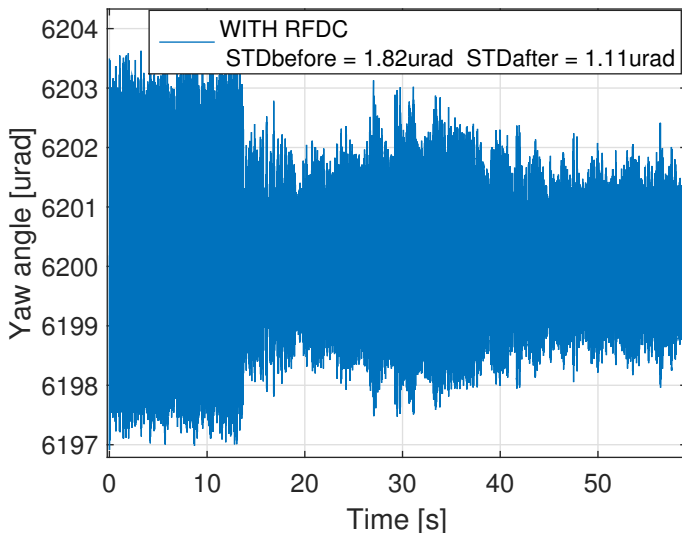


**Figure 5.7:** Closed loop transient showing the response of the activation of the RFDC. Cancellation of the 50 Hz environmental disturbances.

### 5.2.2 Multiple Disturbances

The cancellation of several disturbances simultaneously was verified by trying to cancel out a 50 Hz component originating from environmental disturbances in the laboratory and a 80 Hz generated by the shaker. Figure 5.8 shows the FFT of the first 10 seconds before and after the cancellation is applied. More data was acquired during the measurement but since the system suffers from the "beat effect" only the first 10 seconds were picked out in order to show the controller ability. During this period of time the 50 Hz component was reduced by 75% and the 80 Hz component by 66% as seen in the figure and its corresponding tables.

The major advantage with the RFDC is that it has the ability to select specific frequencies. To prove this, another test was performed only canceling the 50 Hz component. The result can be seen in Figure 5.9, where it is obvious that the 80 Hz component is not affected by the cancellation of the 50 Hz component.

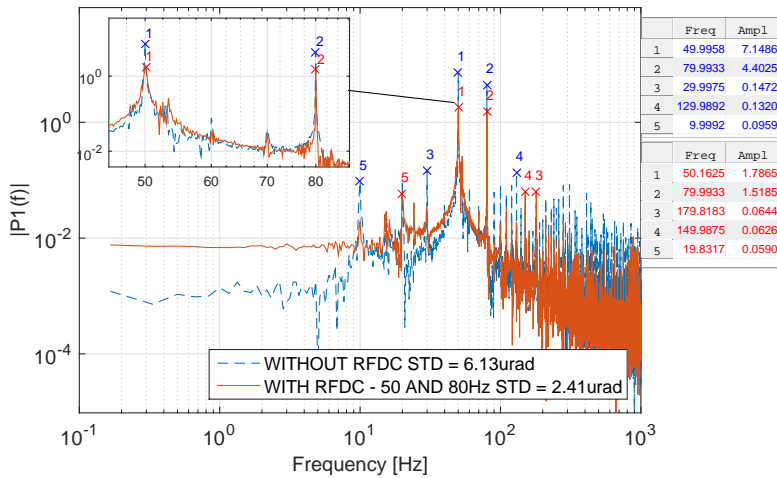


**Figure 5.8:** Multiple cancellation in closed loop of the 50 and the 80 Hz component. The plot is based on a 10 s long acquisition.

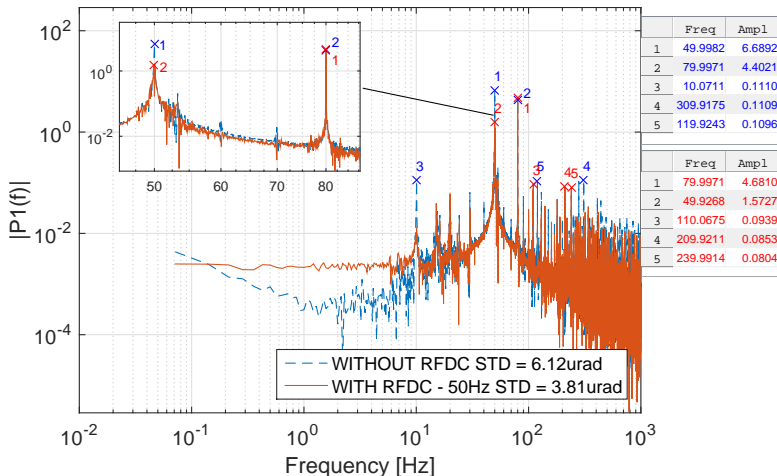


**Figure 5.9:** Cancellation in closed loop of the 50 Hz without affecting the 80 Hz component. The plot is based on a 10 s long acquisition.

### 5.2.3 General Findings

The capturing time, should, if possible be kept as short as possible in order to avoid modeling low frequency behavior. For low frequency disturbance cancellation, a bandpass filter could be considered to be included. Figure 5.10 shows the FFT of the replicated disturbance signal. Optimally this should solely contain the selected frequency and no other components, but as seen in (a) this is not the real case. The effect of an inclusion of a bandpass filter is shown in (b), where the 15 Hz components is filtered out from the other low frequency components. The filter is designed with care to keep zero phase shift for 15 Hz components. However, this filter introduces a phase shift for all other components including the 50 Hz which has shown to imply a reduction of the overall tracking performance.

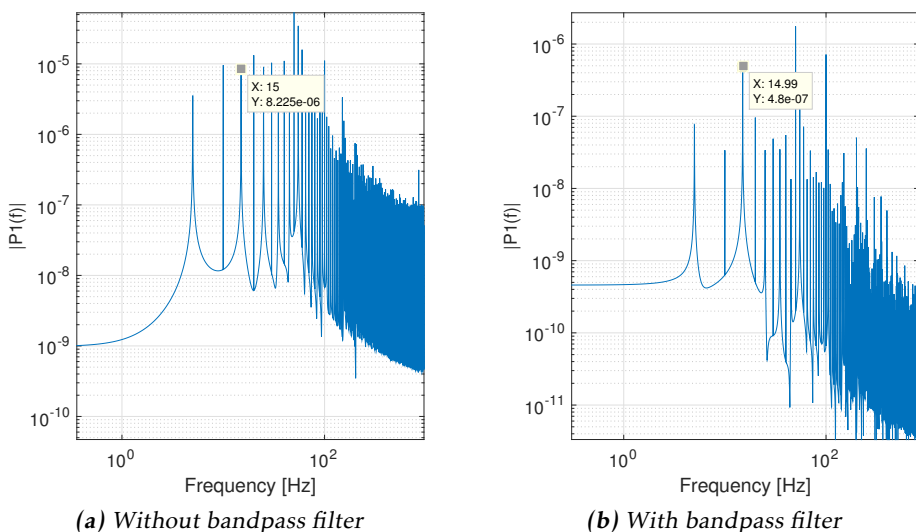


**Figure 5.10:** Effect of filtering the observed disturbance model. The figure shows the FFT of the observed disturbance model where (a) shows the original signal and (b) the filtered signal.

An oscillating effect in the cancellation performance was observed during the measurements. This is known as the "beat effect" and explained in Section 3.3.4. The effect is obvious in Figure 5.11, where the 50 Hz component is only cancelled a fraction of the total acquisition time. According to (3.34), the envelope frequency is half the difference between the two frequencies. The envelope in Figure 5.11 has a period of 50 s giving a beat frequency of 0.04 Hz. To verify that the beat effect was not induced by the algorithm itself, a simple test with two artificial disturbances were performed. Two disturbances were created and injected directly in the program. These frequencies were then set to be cancelled by the RFDC. The result is shown in Figure 5.12 where the standard deviation of the yaw angle displacement can be seen with and without cancellation. The cancellation is here kept constant over 2 minutes, showing no sign of the beat effect.

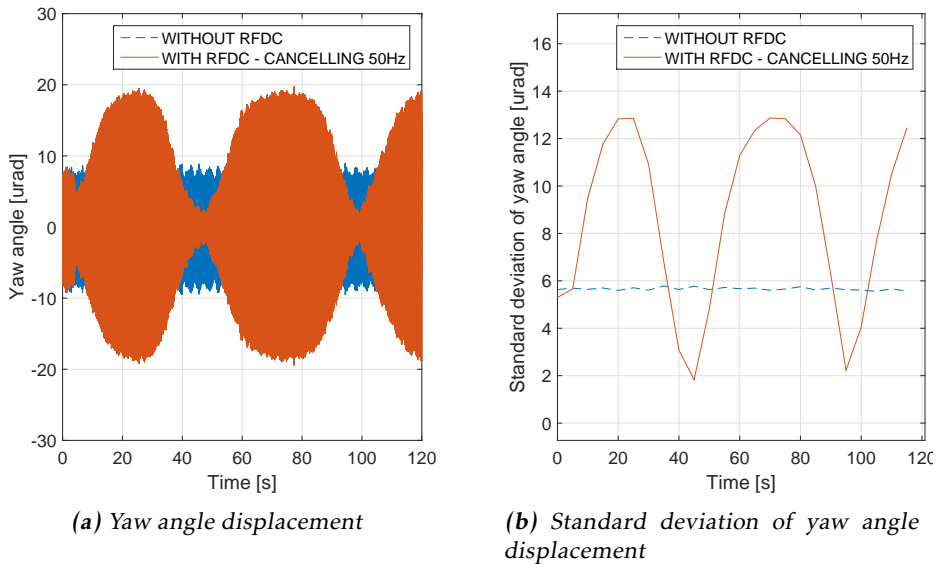


**Figure 5.11:** Cancellation performance in closed loop of the 50 Hz component suffering from the beat effect. The standard deviation, calculated as an average of the standard deviation of (a) every 5 s, is shown in (b).

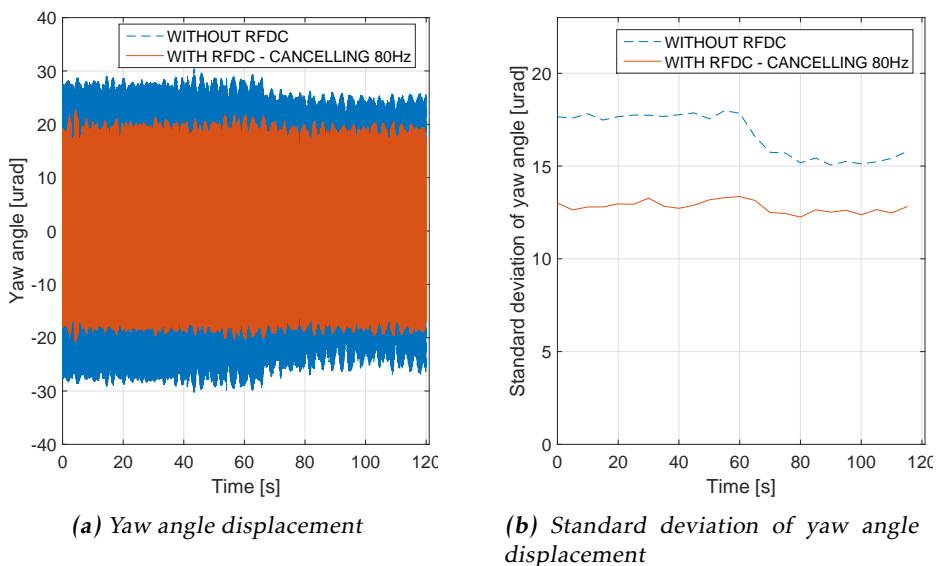


**Figure 5.12:** Cancellation of artificial disturbances in open loop not suffering from beat effect. The yaw angle is shown in (a) with the standard deviation in (b). The change in the data without RFDC is due to environmental changes.

The conspicuous change in the data acquired without the RFDC active, seen at  $t = 60$  s, is due to the environmental changes that were present during the acquisition. However, this change has no impact on the results since the purpose of this test was only to verify that the algorithm provided stable cancellation.

# 6

---

## Conclusion and Future Work

This thesis has investigated different control approaches to improve the tracking capability of a rotational stage used in the UA9 collimation studies at CERN. The investigation has shown that the IRC method can be used to efficiently attenuate the first resonance peak and increase the closed loop bandwidth. It has also shown that the MRACPE can be used to adapt to model changes and prevent instability and that harmonic cancellation can be used to efficiently damp out known harmonic oscillations. Finally a feedforward harmonic cancellation method (RFDC) was implemented and proposed as an add-on control algorithm. This algorithm was first introduced for the control of hard disks but has in this thesis shown to be effective with resonant, piezo-actuated stages as well.

### 6.1 Conclusions

The results gathered during the simulations and the implementation of the RFDC are discussed below. The findings made in this thesis are presented with respect to the results presented in Chapter 4 and 5, highlighting theoretical and practical considerations.

#### 6.1.1 Simulations

##### **IRC and MRACPE**

The comparison presented in Section 4.6 summarizes the simulation results. Looking at Table 4.5, none of the control approaches are globally superior to another but the IRC is the most promising one with respect to the trade-off between tracking accuracy, sensitivity to model errors, stability issues and implementation considerations. The IRC handles severe model errors corresponding to a first resonance peak being moved from its original position in 38.1 Hz to 22 Hz and 67.2

Hz, respectively. The model changes are by far more significant than the results presented in Figure 4.1a, depicting the model's yaw angular dependence, meaning that the IRC would be robust to these variations. Worth mentioning is also that the present controller has shown to be robust to the identified and more realistic model changes (the table only shows the resonance values where one approach becomes unstable). However, for more significant model changes originating from e.g. aging of the piezo stack, the IRC could be advantageous.

In this context and for low angular rates, the adaptive controller has shown good results. However, the adaptive controller has shown drawbacks in many other aspects such as stability and disturbance rejection as outlined in the table. Instability can be caused if the controller has a too high gain with respect to the step size that is applied as input. This nonlinear phenomenon was observed in simulations without any saturation of the input signal, indicating that the amplitude dependent behavior shown in Figure 4.3 might be due to numerical errors. A higher sampling rate would, if not solve the problem completely, at least enhance the border to instability. Another way to maintain stability is to select the initial values more wisely to obtain a quicker convergence without increasing the gain. Figure 4.5 shows the adaptive performance of a periodic input, showing that the controller performs much better for the second period when the parameters are closer to their final value. Considering these issues, the adaptive controller might be better for being used as a secondary controller for long term parameter adaption, at least for operation at 2 kHz.

The major advantage of the IRC is that it attenuates the first resonance peak, allowing for a higher bandwidth but also that this attenuation follows, at least in some extent, the changes in the resonance peak. The negative feedforward gain impacts on the placement of the interlacing zeros, but the placement is also highly dependent on the system itself, since it is in closed loop with the gain. With its higher bandwidth the IRC outperformed the present controller in tracking accuracy as shown in Aspect 3 in Table 4.5. However, neither the present nor the IRC eliminates the constant ramp tracking error completely due to the lack of a double integrator in the controller. A high bandwidth also implies a controller that is more sensitive to measurement noise and to model errors in terms of stability. Considering the fact that the yaw angle measurement is done by interfering with light in ultra high vacuum, there is no significant measurement noise to be taken into account.

### **Harmonic cancellation**

To increase the tracking accuracy even further, the IRC could be used in combination with a harmonic cancellation algorithm. The simulations in this thesis has shown that the RFDC could be a good candidate for cancelling specific harmonic disturbances, especially the ones induced outside the closed loop bandwidth, not reachable by the controller itself. In Table 4.6 the IMP might seem superior at a first glance but this is not the case. The IMP is directly inserted in the closed loop, affecting the closed loop system, deteriorating the sensitivity function and thereby amplifying disturbances with frequencies close to the cancellation fre-

quency. This is not a suitable method for a system containing a lot of induced harmonics closely coupled together as seen in Figure 4.2.

The other two cancellation methods are based on a feedforward approach and do not affect the closed loop system. With respect to cancellation effectiveness with induced model errors (Aspect 3 and 4 in Table 4.6), the FDC is remarkably better than the RFDC. However, this result might be misleading, due to several reasons. Firstly, this approach requires a full model of the disturbance that has to be fed with a known input signal i.e. the disturbance must be known in quite a large extent. Secondly, the FDC performance is only evaluated over one step and only works with a low step rate as input. If the step rate is too high the response could be interfering with other step responses making the disturbance even harder to model.

Considering the above with the goal to cancel out harmonic oscillations, the RFDC is the most preferable approach. It allows for cancellation of known harmonic disturbances while it only uses the angular measurement and the given output at the time to estimate the correct phase and amplitude of the disturbance. The observer converge time must be carefully estimated. In the simulations it was confirmed that the a quicker convergence implies more noise added to the observed model, especially for high frequency models with frequencies close to the Nyquist frequency. The addition of a bandpass filter has not shown any increase of the cancellation performance. The problem lies in the fact that unmodeled disturbances that enter the disturbance estimation become phase-shifted by the filter which lead to an amplification of their frequency components.

### 6.1.2 Implementation

The RFDC implementation showed good results, overall consistent with the results from the simulations. Cancellation was verified both in open and closed loop and with the selection of single and multiple disturbances. One important result is shown in Figure 5.9, where the 50 Hz is canceled without affecting the 80 Hz component. This also shows that environmental disturbances (not generated by the shaker), can be effectively reduced by this implementation. The environmental disturbance level in the lab was much higher than the expected level of disturbance in the tunnel. This implied a standard deviation varying between 1  $\mu\text{rad}$  and 10  $\mu\text{rad}$  in closed loop operation. Such a large varying standard deviation makes it difficult to compare two tests with each other. Hence, the reduction of the yaw angle shown in for instance Figure 5.5 should be seen as an indication of the harmonic cancellation capability. This also explains the big difference between the open and closed loop performance, shown in Figure 5.2 and Figure 5.4, which in theory should have the same cancellation performance after the response has settled.

The implementation also showed an effect that was not captured in the simulations, i.e. the "beat effect" showing as an oscillation in the cancellation performance. This undesirable effect must be overcome before this algorithm can be implemented on the real controller that operates in the LHC tunnel. Solutions that could possibly mitigate this effect are discussed in the following section.

In its current state, the implementation does not fulfill all goals stated in Section 1.3 but it proves the harmonic cancellation concept. With some further development it will become a valuable resource to achieve the stated goals in future.

## 6.2 Future Work

In the future, the tracking capability could be enhanced even further by combining some of the methods used in this thesis. For example to increase bandwidth and tracking capability the IRC could be implemented, and for the rejection of specific induced harmonics, the RFDC could be used without deteriorating the sensitivity to disturbances and model errors. Also an adaptive approach might be valuable to measure and adapt the controller parameters to long term effects such as thermal effects and aging of the piezoelectric actuator.

Improvement in the mechanical design could also be done. In fact, a new, high stiffness rotational stage has already been manufactured to increase the overall stiffness and thereby also extending the bandwidth, allowing for more precise tracking and better disturbance rejection. Even though it has a higher bandwidth than the previous stage, different angular and linear operating points still change the linear model drastically. The IRC is a promising control technique for handling these type of model changes (at least up to some extent) since it only uses a negative feedforward to damp out the first resonance peak and has no direct information of where the first resonance peak may be located. However, further investigation has to be carried out in order to gain a better knowledge about the controller robustness to high order model changes and techniques that can be used to be more robust to them.

To improve the already implemented RFDC method, several adjustments can be made. For instance, a big drawback is that the frequencies that can be selected for cancellation must have an integer number of periods that is a multiple of the sampling time. To achieve intersample disturbance rejection, a multi rate control technique with a control period shorter than the sampling period can be implemented, as proposed in [11]. Another improvement would obviously be to get rid of the beat effect. The effect could be mitigated by using some technique that regularly synchronizes the observed disturbance with the replicated one. One way could be to observe the disturbance at all time and only use a few elements to synchronize the phase of the replicated disturbance, but how this technique would work in its full is left for future investigation.

# **Appendix**



# A

---

## Simulation values

### A.1 RFDC

$$\mathbf{A}_{zs} = \begin{bmatrix} 1.8460 & -0.5465 & -0.0080 & 0.6575 & -0.7755 & 0.4758 \\ 2.0000 & 0 & 0 & 0 & 0 & 0 \\ 0 & 1.0000 & 0 & 0 & 0 & 0 \\ 0 & 0 & 0 & 1.0000 & 0 & 0 \\ 0 & 0 & 1.0000 & 0 & 0 & 0 \\ 0 & 0 & 0 & 0 & 0.5000 & 0 \end{bmatrix} \quad (\text{A.1a})$$

$$\mathbf{B}_{zs} = \begin{bmatrix} 0.1250 \\ 0 \\ 0 \\ 0 \\ 0 \\ 0 \end{bmatrix} \quad (\text{A.1b})$$

$$\mathbf{C}_{zs} = \begin{bmatrix} 0.1253 & -0.0204 & 0.0254 & -0.0021 & 0.0277 & 0 \end{bmatrix} \quad (\text{A.1c})$$

## A.2 Feedforward Disturbance Cancellation

$$P_d(z) = \frac{a_1 z^{-1} + \dots + a_{19} z^{-19}}{b_0 + b_1 z^{-1} + \dots + b_{20} z^{-20}} \quad (\text{A.2})$$

| $i$   | 0   | 1     | 2     | 3    | 4     | 5    | 6    | 7    | 8    | 9    | 10    |
|-------|-----|-------|-------|------|-------|------|------|------|------|------|-------|
| $a_i$ | -   | -0.23 | -4.5  | 16.1 | -17.6 | 1.1  | 17.1 | 21.7 | 7.5  | 14.0 | -19.9 |
| $b_i$ | 1   | -2.8  | 1.7   | 2.9  | -5.6  | 3.1  | 2.6  | -7.4 | 5    | 3.2  | -7.2  |
| $i$   | 11  | 12    | 13    | 14   | 15    | 16   | 17   | 18   | 19   | 20   | -     |
| $a_i$ | 3.6 | 17.2  | -23.3 | 13.5 | 1.25  | -9.7 | 9.0  | -4.6 | 1.14 | -    | -     |
| $b_i$ | 3.7 | 1.5   | -4    | 2.9  | 0.49  | -1.9 | 0.67 | 0.05 | 0.14 | 0.10 | -     |

**Table A.1:** Transfer function parameters of  $P_d(z)$

---

## Bibliography

- [1] Sumeet S Aphale, Andrew J Fleming, and SO Reza Moheimani. Integral control of smart structures with collocated sensors and actuators. In *Control Conference (ECC), 2007 European*, pages 2595–2602. IEEE, 2007. Cited on pages 21 and 22.
- [2] Giustiniani A. Masi A. Biggio M., Butcher M. and Storace M. Memory characteristics of hysteresis and creep in multi-layer piezoelectric actuators: An experimental analysis. *Physica B: Condensed Matter*, 435:40–43, 2014. Cited on page 3.
- [3] Giustiniani A. Butcher M. and Masi A. On the identification of hammerstein systems in the presence of an input hysteretic nonlinearity with nonlocal memory: Piezoelectric actuators – an experimental case study. *Physica B: Condensed Matter*, pages 1—5, 2015. Cited on pages 3, 12, and 13.
- [4] Losito R. Butcher M., Giustiniani A. and Masi A. Controller design and verification for a rotational piezo-based actuator for accurate positioning applications in noisy environments. *Iecon 2015*, 2015. Cited on pages 3, 12, 13, and 16.
- [5] Ning Chuang, Ian R Petersen, and Hemanshu R Pota. Robust h-inf control in fast atomic force microscopy. *Asian Journal of Control*, 15(3):872–887, 2013. Cited on page 3.
- [6] Eleftheriou E. Devasia S. and Moheimani R. A survey of control issues in nanopositioning. *IEEE Transactions on Control Systems Technology*, 15(5):802—823, 2007. Cited on pages 1 and 3.
- [7] Eleftheriou E. Devasia S. and Moheimani R. Piezoelectrics in positioning. tutorial on piezotechnology in nanopositioning applications. *Physik Instrumente (PI) GmbH and Co. KG.*, Retreived in January 2008. URL [http://www.physikinstrumente.com/en/pdf\\_extra/2009\\_PI\\_Piezo\\_University\\_Designing\\_with\\_Piezo\\_Actuators\\_Tutorial.pdf](http://www.physikinstrumente.com/en/pdf_extra/2009_PI_Piezo_University_Designing_with_Piezo_Actuators_Tutorial.pdf). Cited on pages 1, 3, and 11.

- [8] Bojana Drincic. *Mechanical models of friction that exhibit hysteresis, stick-slip, and the Stribeck effect*. PhD thesis, The University of Michigan, 2012. Cited on page 3.
- [9] N. Elmali H., Olgac. Implementation of sliding mode control with perturbation estimation (smcpe). *IEEE Transactions on control system technology*, 4 (5), 1996. Cited on pages 3 and 18.
- [10] Gunnarsson S. Lindskog P. Ljung L. Löfberg J. McKelvey T. Stenman A. Strömberg J-E. Enqvist M., Glad T. *Industriell reglerteknik Kurskompendium*. Reglerteknik, Institutionen för systemteknik, second edition, 2014. Cited on pages 23 and 26.
- [11] Hiroshi Fujimoto. Rro compensation of hard disk drives with multirate repetitive perfect tracking control. *IEEE Transactions on Industrial Electronics*, 56(10):3825–3831, 2009. Cited on pages 3, 23, 25, and 78.
- [12] Hiroshi Fujimoto, F Kawakami, and S Kondo. Repetitive control of hard disk drives based on switching scheme: Experimental verification for multiple mode disturbance. In *Advanced Motion Control, 2004. AMC'04. The 8th IEEE International Workshop on*, pages 323–328. IEEE, 2004. Cited on pages 23, 25, and 27.
- [13] Ljung L. Glad T. *Reglerteorি*. Studentlitteratur AB, second edition, 2003. Cited on pages 19, 23, and 53.
- [14] Guo-Ying Gu, Li-Min Zhu, Chun-Yi Su, and Han Ding. Motion control of piezoelectric positioning stages: modeling, controller design, and experimental evaluation. *IEEE/ASME Transactions on Mechatronics*, 18(5):1459–1471, 2013. Cited on page 3.
- [15] Guo-Ying Gu, Li-Min Zhu, and Chun-Yi Su. Integral resonant damping for high-bandwidth control of piezoceramic stack actuators with asymmetric hysteresis nonlinearity. *Mechatronics*, 24(4):367–375, 2014. Cited on pages 3 and 21.
- [16] Guo-Ying Gu, Li-Min Zhu, Chun-Yi Su, Han Ding, and Sergej Fatikow. Modeling and control of piezo-actuated nanopositioning stages: a survey. *IEEE Transactions on Automation Science and Engineering*, 13(1):313–332, 2016. Cited on page 3.
- [17] Kam K Leang and Santosh Devasia. Hysteresis, creep, and vibration compensation for piezoactuators: Feedback and feedforward control. In *Proceedings of the Second IFAC Conference on Mechatronic Systems, Berkeley, CA, Dec*, pages 9–11. Citeseer, 2002. Cited on page 3.
- [18] Daniele Mirarchi. *Crystal collimation for LHC*. PhD thesis, Imperial Coll., London, 2015. Cited on page 2.

- [19] Kok K. T. Qingsong X. *Advanced Control of Piezoelectric Micro-/Nanopositioning Systems*. Springer International Publishing, first edition, 2016. Cited on pages 11, 18, and 19.
- [20] MS Rana, HR Pota, IR Petersen, et al. Control of resonant modes of a smart structure using ompc. In *2013 9th Asian Control Conference (ASCC)*, 2013. Cited on page 3.
- [21] Liu X. Sun Y. Ru C. *Nanopositioning Technologies*. Springer International Publishing, first edition, 2016. Cited on page 13.
- [22] W Scandale, G Arduini, M Butcher, F Cerutti, M Garattini, S Gilardoni, A Lechner, R Losito, A Masi, D Mirarchi, et al. Observation of channeling for 6500 gev/c protons in the crystal assisted collimation setup for lhc. *Physics Letters B*, 758:129–133, 2016. Cited on page 2.
- [23] Sydney Australia UNSW, School of Physics. Interference beats and tar-tini tones, Retreived in August 2016. URL <http://www.animations.physics.unsw.edu.au/jw/beats.htm>. Cited on page 28.
- [24] Ramon Vilanova, Orlando Arrieta, Asier Ibeas, Pedro Balaguer, and Carles Pedret. Disturbance compensation on uncertain systems: Feedforward control design for stable systems. *IFAC Proceedings Volumes*, 41(2):11310–11315, 2008. Cited on pages 3 and 23.
- [25] Qingsong Xu and Minping Jia. Model reference adaptive control with perturbation estimation for a micropositioning system. *IEEE Transactions on control systems technology*, 22(1):352–359, 2014. Cited on page 3.
- [26] Mei-Ju Yang, Guo-Ying Gu, and Li-Min Zhu. High-bandwidth tracking control of piezo-actuated nanopositioning stages using closed-loop input shaper. *Mechatronics*, 24(6):724–733, 2014. Cited on page 3.
- [27] Perry Y.Li. Internal model principle and repetitive control, ch 8, Retreived in June 2016. URL <http://www.me.umn.edu/courses/me8281/notes/ Old%20S06/Chapter%208%20IMP-repetitive.pdf>. Cited on pages 3 and 24.